Determination of Gravitational Wave Event Parameters with the future Einstein Telescope using Bayesian Estimation

Sander Lindelauf

Masterarbeit in Physik

vorgelegt der
Fakultät der Mathematik, Informatik und Naturwissenschaften
der RWTH Aachen

im August 2021
angefertigt am

III. Physikalischen Institut A

1. Prüfer: Prof. Thomas Hebbeker
2. Prüfer: Prof. Achim Stahl

Contents

1 Introduction

This work wish to investigate how well one can reconstruct gravitational wave parameters and wether it is possible to measure cosmological parameters using gravitational wave events without any electromagnetic counterpart. This chapter will introduce gravitational waves, some basics of cosmology and a toy model. Chapter 2 will discuss the model used to analyse and simulate gravitational waves (GWs). Chapter 3 describes how detectors work and how to simulate realistic results. Having both a model and data one can start by talking about how to analyse the simulated data. The algorithm used will be described in chapter 4 and in chapter 5 the results attained using the previously described method will be discussed. Lastly in this work geometric units are used to simplify formulae, meaning $G = c = 1$.

1.1 Gravitational Waves

Einstein published his final paper on General Relativity in 1915[1]. In his theory of general relativity he replaced a force of gravity like in Newton's theory of gravity by curved spacetime where the curvature is caused by massive objects. When working on the weak field limit he found there was a possibility for gravitational waves which he published in 1918[2]. This was first to believed to be either an unphysical solution or so small that it would be impossible to measure, however in 2015 gravitational waves were measured for the first time using the LIGO observatory in Hanford and Livingston[3].

1.2 ΛCDM

In 1929 Edwin Hubble published his famous paper[4] about the discovery of a linear dependence between the distance of stars and the corresponding velocity. In fig. 1.1 one can see his original data where the velocity increases at greater distances. This baffled scientists at

[1] Albert Einstein. Die Feldgleichungen der Gravitation. *Sitzungsberichte der Königlich Preußischen Akademie der Wissenschaften Berlin*, pages 844–847, Jan 1915

[2] Albert Einstein. Über Gravitationswellen. *Sitzungsberichte der Königlich Preußischen Akademie der Wissenschaften (Berlin)*, pages 154–167, Jan 1918

[3] LIGO Scientific Collaboration. Observation of Gravitational Waves from a Binary Black Hole Merger. *Physical Review Letters*, 116(6), Feb 2016. DOI: 10.1103/PhysRevLett.116.061102

[4] Edwin Hubble. A Relation Between Distance and Radial Velocity Among Extra-Galactic Nebulae. *Proceedings of the National Academy of Sciences*, 15(3):168–173, Mar 1929. DOI: 10.1073/pnas.15.3.168

first as many believed that the universe was infinitely old and static, so such movements would suggest that the universe is expanding. In the meantime both Friedmann[5] and Lemaître [6] used Einstein's theory of general relativity to describe an expanding universe.

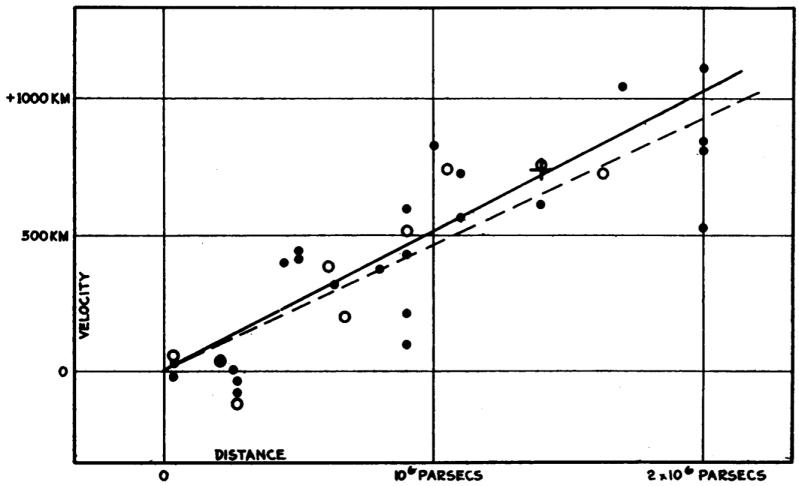

FIGURE 1

[5] A. Friedmann. Über die Krümmung des Raumes. *Zeitschrift für Physik*, 10(1):377–386, Dec 1922. DOI: 10.1007/BF01332580

[6] G. Lemaître. Un Univers homogène de masse constante et de rayon croissant rendant compte de la vitesse radiale des nébuleuses extra-galactiques. *Annales de la Société Scientifique de Bruxelles*, 47: 49–59, Jan 1927

Figure 1.1: Plot from [Hubble, 1929] one sees a clear correlation between distance and (radial) velocity. The Hubble parameter was estimated to be around $H \approx 500\ \mathrm{km\,s^{-1}Mpc^{-1}}$ for this first measurement.

In order to describe this expansion one will first need to describe spacetime. In order to do this the line element is used, which describes the distance between two events in spacetime. The line element ds is defined as:

$$ds^2 = dx^\mu dx^\nu g_{\mu\nu} \tag{1.1}$$

dx^μ describes an infinitesimal change in direction μ whereas $g_{\mu\nu}$ describes the line element in a specific coordinate system. The line element is invariant under changes of coordinate system, so it is the same for all observers. Assuming flat spacetime this line element is written as $ds^2 = -dt^2 + dx^2 + dy^2 + dz^2$ [7]. If $ds^2 > 0$ these events are spacelike meaning that no light could have travelled between these events. In this case the line element corresponds to the proper distance i.e. the distance an observer would measure between these events. On the other hand if $ds^2 < 0$ the events are timelike meaning massive particles could have travelled between these events. In this case the line element corresponds to the proper time i.e. the time difference an observer would measure between these events. The line element of an expanding universe as is written as: [8]

$$ds^2 = d\tau^2 = -dt^2 + a^2(t)\left[\vec{dx}^2 + K\frac{(\vec{x}\cdot\vec{dx})^2}{1 - K\vec{x}^2}\right] \tag{1.2}$$

[7] In this case $g_{\mu\nu} = \mathrm{diag}(-1,1,1,1) = \eta_{\mu\nu}$.

[8] for more information see Steven Weinberg. *Cosmology*. Oxford University Press, 2008

where $a(t)$ is the scale factor, which is explained in fig. 1.2. Assuming the points themselves do not move, the space surrounding them expands and therefore the distance between them increases. Consequently one can also perceive a speed between these points if the scale factor increases. K is the curvature factor and is $K \in \{-1, 0, 1\}$. If $K = 1$ is curved positively and will want to collapse, if $K = -1$ the universe is curved negatively and will want to keep expanding, finally if $K = 0$ the universe is flat and has no preference.

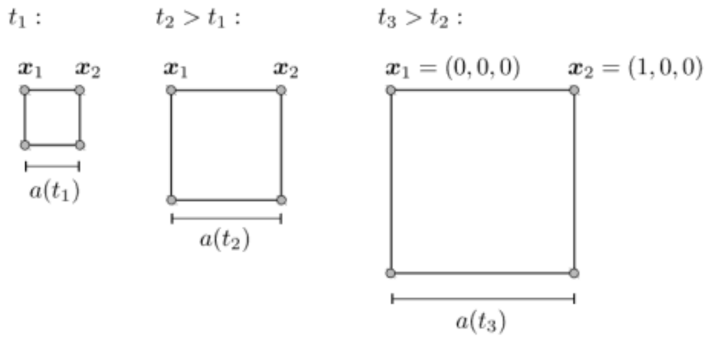

Figure 1.2: Sketch explaining expansion of the universe. The coordinate system remains the same however distances between points increases due to the increase of $a(t)$. [Dodelson, 2003]

In the used metric the proper distance[9] is given by:

$$d(r,t) = a(t) \int_0^r \frac{dr}{1 - Kr^2} = a(t) \times \begin{cases} \arcsin r, & K = +1 \\ r & K = 0 \\ \operatorname{arcsinh} r & K = -1 \end{cases} \tag{1.3}$$

[9] The distance one would measure at a specific moment of cosmological time

Using this the change in proper distance can also be written as:

$$\frac{d}{dt} d(r,t) = d(r,t) \frac{\dot{a(t)}}{a(t)} = d(r,t) H(t) \tag{1.4}$$

Where $H(t)$ is called the Hubble parameter. It can be seen that there is a linear relation between speed and distance. Lastly in this work the reduced Hubble parameter h will be used, which is defined as

$$H(t) = h(t) \times 100 \frac{\text{km}}{\text{s Mpc}} \tag{1.5}$$

As a first measure of distance and the Hubble parameter have been defined, one needs to concern themselves with the dynamics of the cosmos as light takes time to travel. Therefore the state of the universe at an earlier point in time can have an influence on the light observed. Currently the best model to describe the dynamics of the universe is the Λ CDM model, which is based on the work of the aforementioned Friedmann and Lemaître, but also Robertson and Walker [10] [11]. They independently solved Einstein's field equations for a homogeneous universe where the expansion of the universe can be predicted using several densities ρ_i and their specific behaviour. There are three different densities: radiation (e.g.. light, but also highly relativistic particles such as neutrinos), matter (also including dark matter) and vacuum energy or dark energy. These all behave differently if space expands or contracts, radiation loses energy (or cools down) if space expands, therefore the energy density of radiation follows $\rho_r \sim a(t)^{-4}$. Non relativistic matter does not lose energy but disperses and therefore the energy density only goes down as $\rho_m \sim a(t)^{-3}$. Vacuum energy has no dependence on the scale factor and is constant in time. Then using Friedmann's equation [12]:

$$\left(\frac{\dot{a}(t)}{a(t)}\right)^2 = H(t)^2 = \frac{8\pi}{3}\rho - \frac{K}{a(t)^2} \tag{1.6}$$

it is possible to compute the density for which spacetime is flat, this is called ρ_c. The fraction can be defined

$$\Omega_i = \rho_i/\rho_c \tag{1.7}$$

So Ω_r is the fraction for radiation, Ω_m for mass and Ω_Λ for dark energy. Lastly to incorporate curvature the sum of the fractions is set to 1 meaning $\Omega_k = 1 - \Omega_r - \Omega_m - \Omega_\Lambda$ and following eq. 1.6 Ω_k is proportional to $a(t)^{-2}$. The evolution of the Hubble parameter can then be written as [13]

$$H(t)^2 = H(t_0)^2 \left[\Omega_r \left(\frac{a(t)}{a(t_0)}\right)^{-4} + \Omega_m \left(\frac{a(t)}{a(t_0)}\right)^{-3} + \Omega_k \left(\frac{a(t)}{a(t_0)}\right)^{-2} + \Omega_\Lambda\right] \tag{1.8}$$

In this equation the subscript 0 denotes at the present. Current measurements suggest that $\Omega_r \approx 0$, $\Omega_m \approx 0.3$, $\Omega_k \approx 0$ and $\Omega_\Lambda \approx 0.7$.[14]

Redshift

To calculate the Hubble parameter one needs both the perceived velocity and the distance to an object. How to measure distances is outside the scope of this thesis. However the velocity can be calculated through the redshift of light emitted by stars in a system. One

[10] H. P. Robertson. Kinematics and World-Structure. *The Astrophysical Journal*, 82:284, Nov 1935. DOI: 10.1086/143681

[11] A. G. Walker. On Milne's Theory of World-Structure. *Proceedings of the London Mathematical Society*, s2-42(1): 90–127, Jan 1937. DOI: 10.1112/plms/s2-42.1.90

[12] A. Friedmann. Über die Krümmung des Raumes. *Zeitschrift für Physik*, 10(1):377–386, Dec 1922. DOI: 10.1007/BF01332580

[13] Steven Weinberg. *Cosmology*. Oxford University Press, 2008

[14] N. Aghanim, Y. Akrami, M. Ashdown, J. Aumont, C. Baccigalupi, and et al. Planck 2018 results. *Astronomy and Astrophysics*, 641:A6, Sep 2020. DOI: 10.1051/0004-6361/201833910

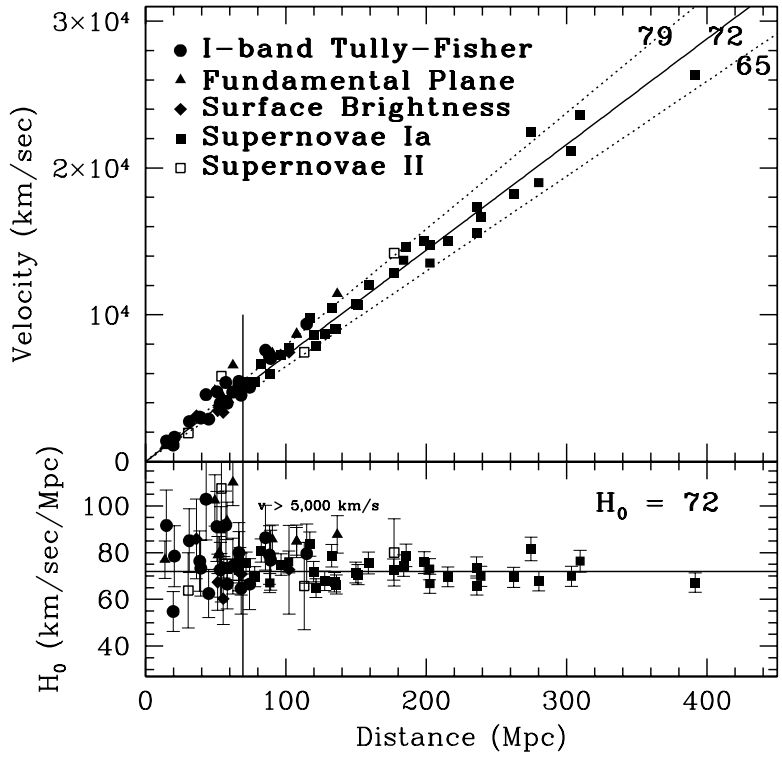

Figure 1.3: Distance-velocity plot from the Hubble Space Telescope. Compared to fig. 1.1 the distances are up to a factor of 10^2 higher than used by Hubble. Taken from [Freedman et al., 2001]

can identify spectral lines where the wavelength λ_0 at emission is known and compare this to the measured wavelength λ. The particular speed of a star will cause a redshift caused by the electromagnetic doppler effect. Even though this is difference is relatively small it can be measured very well. For the largest part redshift will be dominated by the expansion of the universe, where light loses energy due to this expansion[15]. The redshift is defined as

$$1 + z \equiv \frac{\lambda}{\lambda_0} = \frac{a(t)}{a(t_0)} \tag{1.9}$$

Here t_0 is the time of emission and t is the time at which the wave is observed.

[15] See [Weinberg, 2008] for more information

Hubble Tension

Currently the Hubble parameter is believed to be around $70\mathrm{km\,s^{-1}Mpc^{-1}}$ which is vastly different to Hubble's first measurement of $500\mathrm{km\,s^{-1}Mpc^{-1}}$. In fig. 1.4 and fig. 1.5 one can see how measurements of the Hubble parameter evolved in time. After around 1960 values start to converge around the current value. Partly responsible for the difference

between Hubble's first measurement and current measurements is the short distances used where the particular speed of galaxies might dominate the redshift which is measured. The difference can for instance be seen in fig. 1.3 where the largest distance is a factor of 200 times further away compared to Hubble's first measurement in fig. 1.1. In the meantime the Hubble parameter has also been inferred from the Cosmic Microwave Background (CMB) using the PLANCK telescope [16] which yielded $H_0 = 67.4 \pm 0.5 \mathrm{km\,s^{-1}Mpc^{-1}}$ and by observing supernovae type 2a and Cepheids which resulted in $H_0 = 74.03 \pm 1.42 \mathrm{km\,s^{-1}Mpc^{-1}}$ [17]. This is a difference over 4σ and this difference is called the Hubble Tension, which can be seen best in fig. 1.5.

In 1986 Schutz proposed using gravitational waves in order to measure the Hubble parameter [18]. An advantage of measuring gravitational waves and using them as "Standard Sirens" is that one can infer the distance directly from the amplitude as will be discussed in more detail in chapter 2. If precise enough this could help to answer the question whether this so-called Hubble tension is caused by a mistake in either measurement or if the cosmological model might be incorrect.

[16] N. Aghanim, Y. Akrami, M. Ashdown, J. Aumont, C. Baccigalupi, and et al. Planck 2018 results. *Astronomy and Astrophysics*, 641:A6, Sep 2020. DOI: 10.1051/0004-6361/201833910

[17] Adam G. Riess, Stefano Casertano, Wenlong Yuan, Lucas M. Macri, and Dan Scolnic. Large Magellanic Cloud Cepheid Standards Provide a 1the Determination of the Hubble Constant and Stronger Evidence for Physics beyond Lambda CDM. *The Astrophysical Journal*, 876(1), May 2019. DOI: 10.3847/1538-4357/ab14422

[18] Bernard F. Schutz. Determining the Hubble constant from gravitational wave observations. *Nature*, 323(6086):310–311, Sep 1986. DOI: 10.1038/323310a0

Cosmological Distances

There are several distances important in cosmology and astronomy. The one most interesting for this work are the luminosity distance D_L and the co-moving distance D_C. The luminosity distance D_L is

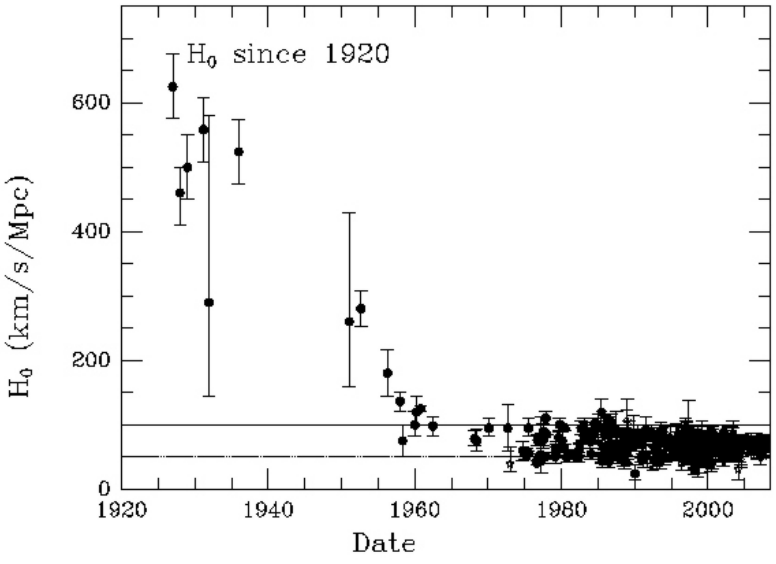

Figure 1.4: Evolution of measurements of the Hubble parameter from 1920 to 2000. From around 1960 the values converge towards around 70 $\mathrm{kms^{-1}Mpc}-1$.Taken from [Huchra]

defined by the relationship between apparent luminosity l and the absolute luminosity L:

$$l = \frac{L}{4\pi {D_L}^2} \tag{1.10}$$

The co-moving distance D_C can be calculated using

$$D_C(z) = \frac{c}{H_0} \int_0^z dz' \frac{1}{\sqrt{\Omega_r (1+z')^4 + \Omega_m (1+z')^3 + \Omega_k (1+z')^2 + \Omega_\Lambda}} \tag{1.11}$$

The luminosity distance is calculated using the co-moving distance [19]

$$D_L = (1+z) \begin{cases} \frac{c}{H_0\sqrt{-\Omega_k}} \sin\left(\frac{H_0\sqrt{-\Omega_k} D_C(z)}{c}\right) & \Omega_k < 0 \\ D_C(z) & \Omega_k = 0 \\ \frac{c}{H_0\sqrt{\Omega_k}} \sinh\left(\frac{H_0\sqrt{\Omega_k} D_C(z)}{c}\right) & \Omega_k > 0 \end{cases} \tag{1.12}$$

[19] Steven Weinberg. *Cosmology*. Oxford University Press, 2008

1.3 *Weak Field Approximation*

To understand how gravitational waves work one needs the Einstein equation. It governs how gravitational fields behave and goes as follows

$$G_{\mu\nu} + \Lambda g_{\mu\nu} = 8\pi T_{\mu\nu} \tag{1.13}$$

Here $G_{\mu\nu}$ is the Einstein tensor, Λ is the cosmological constant[20], $g_{\mu\nu}$ is the metric tensor and $T_{\mu\nu}$ is the stress-energy tensor. As the effects

[20] Dark energy will not have a significant effect on gravitational waves apart from redshift through the expansion of space.

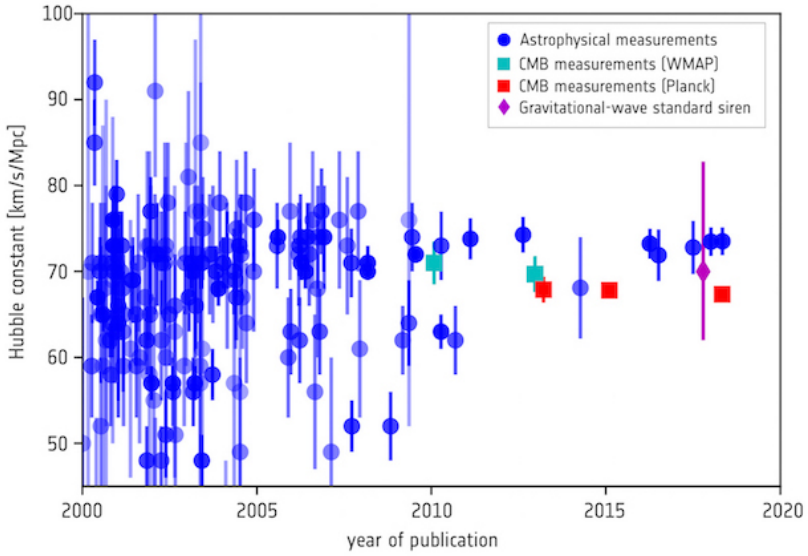

Figure 1.5: Evolution of measurements of the Hubble parameter after 2000 for several sources. The dark blue measurements have been made using astrophysical objects like supernovae and cepheids. The light blue measurements were measurements of the cosmic microwave background using the WMAP telescope. After 2015 the CMB had been measured more precise, however with these new values it was no longer compatible with astrophysical measurements. Taken from [ESA/Planck Collaboration]

of gravitational waves are expected to be small on earth it can be presumed that metric tensor can be written as

$$g_{\mu\nu} = \eta_{\mu\nu} + h_{\mu\nu} \tag{1.14}$$

where $\eta_{\mu\nu}$ is the metric for flat spacetime and $h_{\mu\nu} \ll 1$ is a small perturbation. Meaning eq. 1.13 can be rewritten for this small perturbation as

$$\Box \bar{h}_{\mu\nu} = -16\pi T_{\mu\nu} \tag{1.15}$$

Where $\bar{h}_{\mu\nu} := h_{\mu\nu} - \eta_{\mu\nu}h/2$ is called the "reverse trace" of $h_{\mu\nu}$ because $h^{\alpha}{}_{\alpha} = -h$. [21]. When moving through a vacuum the stress energy tensor $T_{\mu\nu} = 0$, therefore eq. 1.15 becomes

[21] For more information see [Schutz, 2009]

$$(-\partial_t^2 + \nabla^2)h_{\mu\nu} = 0 \tag{1.16}$$

One possible solution to this differential equation is a transversal wave given by

$$\bar{h}_{\mu\nu} = A_{\mu\nu} \exp(ik_\alpha x^\alpha) \tag{1.17}$$

with the condition $A^{\mu\nu}k_\nu = 0$. Using gauge freedom one can restrict the amplitude tensor more so it is given by

$$A_{\mu\nu} = \begin{pmatrix} 0 & 0 & 0 & 0 \\ 0 & A_+ & A_\times & 0 \\ 0 & A_\times & -A_+ & 0 \\ 0 & 0 & 0 & 0 \end{pmatrix} \tag{1.18}$$

assuming without loss of generality that $k_\mu = (\omega, 0, 0, \omega)$ (meaning the gravitational wave is moving in $\hat{e}_z$-direction.)

Polarisation

Using eq. 1.18 the line element can be written as:

$$ds^2 = -dt^2 + dz^2 + (1 + h_+(t)) \cdot dx^2 + (1 - h_+(t)) \cdot dy^2 + 2h_\times(t)dxdy \tag{1.19}$$

One can recognise two amplitudes corresponding to two polarisations, these are the $+$ and $\times$-polarisations. If one were to rotate the coordinate system by $\pi/4$ around the $\hat{e}_z$ axis the $+$-polarisation becomes the $\times$-polarisation and vice versa.
In fig. 1.6 one can see the effect of a gravitational wave on free particles in the $x - y$ plane. As will be discussed later gravitational waves created by orbiting massive objects will only create linear polarised waves in the plane of orbit, in other directions the waves will be circular or elliptical polarised, meaning a combination of both polarisations. This would mean that the ellipse in fig. 1.6 would seem to rotate.

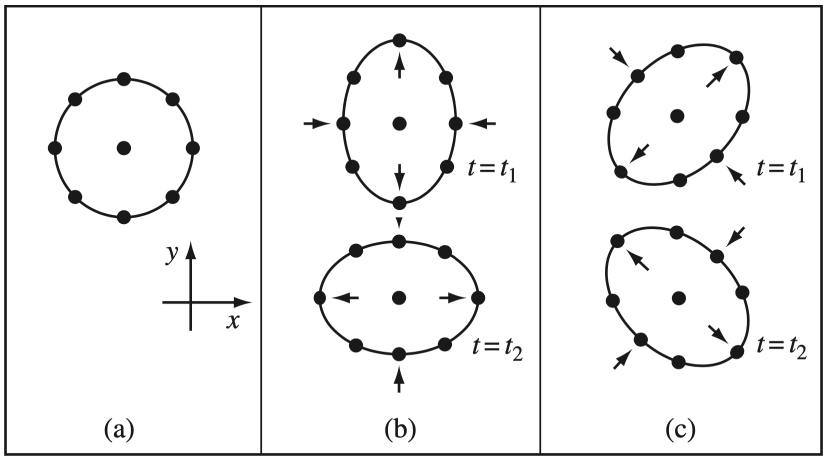

Figure 1.6: Path of free particles in the x_y plane for a gravitational wave moving in the $\hat{e}_z$ direction. In figure (a) there is no gravitational wave. In figure (b) the effect of the $+$-polarisation is shown and in figure (c) the effect of the $\times$-polarisation.[Schutz, 2009]

Quadrupolmoment

In order to solve eq. 1.15 the assumption is made that the stress energy tensor can be written as

$$T_{\mu\nu} = \Re(S_{\mu\nu}e^{-i\Omega t}) \tag{1.20}$$

where $S_{\mu\nu}$ is the time-independent stress energy tensor and Ω is the oscillation frequency. Presuming that both objects are compact (the space where $S_{\mu\nu} \neq 0$ is small compared to the wavelength $2\pi/\Omega$). Using the Ansatz:

$$\bar{h}_{\mu\nu} = B_{\mu\nu}e^{-i\Omega t} \tag{1.21}$$

Using eq. 1.20, eq. 1.15 can be written as:

$$(\nabla^2 + \Omega^2)B_{\mu\nu} = -16\pi S_{\mu\nu} \tag{1.22}$$

The solution to this equation is

$$B_{\mu\nu} = \frac{C_{\mu\nu}}{r}e^{i\Omega r} + \frac{D_{\mu\nu}}{r}e^{-i\Omega r} \tag{1.23}$$

where $C_{\mu\nu}$ is the outgoing wave and $D_{\mu\nu}$ is the ingoing wave. As only the outgoing waves are of interest one sets $D_{\mu\nu} = 0$. The following differential equation can be solved by integrating [22] and yields

$$\bar{h}_{\mu\nu} = 4\left(\int d^3x S_{\mu\nu}\right)\frac{e^{i\Omega(r-t)}}{r} \tag{1.24}$$

It is possible to simplify this further using the quadrupolmoment. This is defined as

$$I^{lm} := \int d^3x T^{00}x^l x^m = D^{lm}e^{-i\Omega t} \tag{1.25}$$

[22] For more details see B. Schutz. *A First Course in General Relativity*. Cambridge University Press, 2009

where $T^{00} \approx \rho$, the Newtonian mass density. This can be used to write eq. 1.24 as

$$\bar{h}_{\mu\nu} = -2\Omega^2 D_{\mu\nu} \frac{e^{i\Omega(r-t)}}{r} \tag{1.26}$$

Lastly the trace free quadrupole moment is defined as

$$I\!\!I_{jk} := I_{jk} - \frac{1}{3}\delta_{jk} I^l{}_l \tag{1.27}$$

Toy Model

To better understand gravitational radiation it is easiest to start by discussing a toy model as described by Schulz [23]. As the amplitude of a gravitational wave will be in some way proportional to it's masses and should fall with r^{-1} one would expect at most an amplitude of the order M/r. For a mass of $M = 10M_\odot \approx 1.5 \cdot 10^4$m and a radius of $r = 1$Mpc $\approx 3 \cdot 10^{25}$m one would expect an amplitude in the order of magnitude of 10^{-21} [24]. This means eq. 1.15 can be used. Presuming there are two point objects of mass m orbiting each other with a total distance of l_0 between them. This means the orbiting frequency is given by

[23] B. Schutz. *A First Course in General Relativity*. Cambridge University Press, 2009

[24] For more info see [Schutz, 2009]

$$\frac{m^2}{l_0^2} = m\omega^2 \left(\frac{l_0}{2}\right) \Rightarrow \omega = \sqrt{\frac{2m}{l_0^3}} \tag{1.28}$$

The coordinates are given by

$$\begin{aligned} x_1 &= \tfrac{l_0}{2}\cos(\omega t) & y_1 &= \tfrac{l_0}{2}\sin(\omega t) \\ x_2 &= -x_1 & y_2 &= -y_1 \end{aligned} \tag{1.29}$$

Using these coordinates, eq. 1.25, eq. 1.27 and setting $\Omega = 2\omega$ one can calculate the reduced quadrupole moment which is given by

$$\begin{aligned} I\!\!I_{xx} &= -I\!\!I_{yy} = \Re(\tfrac{ml_0^2}{4} e^{-2i\omega t}) \\ I\!\!I_{xy} &= \Re(i\tfrac{ml_0^2}{4} e^{-2i\omega t}) \end{aligned} \tag{1.30}$$

Using eq. 1.24 the perturbation $h_{\mu\nu}$ can be calculated. In the case of a wave travelling in the $\hat{e}_z$ direction:

$$\begin{aligned} \bar{h}_{xx} &= -\bar{h}_{yy} = -2\tfrac{ml_0^2\omega^2}{r}\cos(2\omega(r-t)) \\ \bar{h}_{xy} &= 2\tfrac{ml_0^2\omega^2}{r}\sin(2\omega(r-t)) \end{aligned} \tag{1.31}$$

One finds a circularly polarised wave as the observer is looking onto the rotating objects. In the case of a wave travelling in the $\hat{e}_y$ direction an observer would find

$$\bar{h}_{xx} = -\bar{h}_{zz} = \frac{ml_0^2\omega^2}{r}\cos(2\omega(r-t)) \tag{1.32}$$

This wave is linearly polarised. From the used toy model one can learn several things. Firstly the amplitude one measures will be higher if the detector is in line with the angular momentum and the wave is circularly polarised. Secondly the amplitude depends on the distance between two objects, the mass and the distance between objects and observer. Later one can determine the mass using the frequency and this leaves the distance to be determined and this is essential to measuring cosmological parameters.

2
Simulating Events

In order to infer cosmological parameters using simulated events, a model is needed which can be used to simulate an event and detector response. In this chapter the model used will be discussed. Ch. 3 will discuss how to create noise. It is presumed that there is no correlation between noise and the actual signal and that the measured strain h can be written as $h_i = s_i + n_i$ for a specific detector i, where s is the theoretical strain and n is the noise of that specific detector.

2.1 Signal

The model used to describe the inspiral phase of two compact objects is given by two formulae corresponding to both polarisations. These are given by [1]:

$$h_+ = \frac{2\mathcal{M}_z^{5/3}\left[\pi f(t)\right]^{2/3}}{D_L}\left[1 + (\hat{L}\cdot\hat{n})^2\right]\cos\left[\Phi(t)\right] \tag{2.1}$$

and

$$h_\times = \frac{4\mathcal{M}_z^{5/3}\left[\pi f(t)\right]^{2/3}(\hat{L}\cdot\hat{n})}{D_L}\sin\left[\Phi(t)\right] \tag{2.2}$$

The redshifted "chirp mass" is defined as:

$$\mathcal{M}_z := (1+z)\frac{(m_1 m_2)^{3/5}}{(m_1+m_2)^{1/5}} \tag{2.3}$$

Where m_i is the mass of the respective object. The frequency $f(t)$ is defined using the phase $\Phi(t)$:

$$f(t) = \frac{1}{2\pi}\frac{d\Phi(t)}{dt} \tag{2.4}$$

$\hat{L}$ is the normalised angular momentum vector and $\hat{n}$ is a normalised vector pointing to the observer. $(\hat{L}\cdot\hat{n})$ is often written as $\cos\iota$ where ι is the inclination angle. The evolution of the frequency can be

[1] D. E. Holz and S. A. Hughes. Using Gravitational-Wave Standard Sirens. *The Astrophysical Journal*, 629(1):15–22, Aug 2005. DOI: 10.1086/431341

modeled using post newtonian physics. This leads to the following differential equation [2]

$$\frac{df(t)}{dt} = \frac{96}{5\pi\mathcal{M}_z^2}(\pi\mathcal{M}_z f(t))^{11/3} \cdot \left[1 - \left(\frac{743}{336} + \frac{11}{4}\eta\right)(\pi M f(t))^{2/3} + (4\pi - \beta)(\pi M f(t)) + \left(\frac{34103}{18144} + \frac{13661}{2016}\eta + \frac{59}{18}\eta^2 + \sigma\right)(\pi M f(t))^{4/3}\right] \tag{2.5}$$

Here β is the spin orbit parameter, M is the total mass of the binary system and the symmetric mass ratio $\eta = m_1 m_2/(m_1 + m_2)^2$ where m_1 and m_2 are the individual masses of the coalescing objects. Apart from the first term in eq. 2.5, the other terms do not contribute significantly so these terms can dropped and this formula can be rewritten as [3]

$$\mathcal{M}_z = \left(\left(\frac{5}{96}\right)^3 \pi^{-8}(f(t))^{-11}(\dot{f(t)})^3\right)^{1/5}. \tag{2.6}$$

This can be solved analytically, which yields

$$f(t)^{-8/3} = \frac{(8\pi)^{8/3}}{5}\mathcal{M}_z^{5/3}(t_c - t) \tag{2.7}$$

In fig. 2.1 the evolution of the frequency is shown. This is quite similar to the bottom plot in fig. 2.2. This waterfall plot shows what frequencies are most prevalent at a certain point in time.

Comparison to Toy Model

In the toy model described in sec. 1.3 both the masses and frequency enter in the amplitude, however the exponent is different compared to the actual model used. Also in both models the amplitude of a linear polarised wave is half that of a circular polarised wave and in the direction of the angular moment the wave is circular polarised whereas the wave is linearly polarised in the plane of orbit.

[3] B. P. Abbott, R. Abbott, T. D. Abbott, M. R. Abernathy, and F. et al. Acernese. The basic physics of the binary black hole merger GW150914. *Annalen der Physik*, 529(1-2):1600209, Oct 2016. DOI: 10.1002/andp.201600209

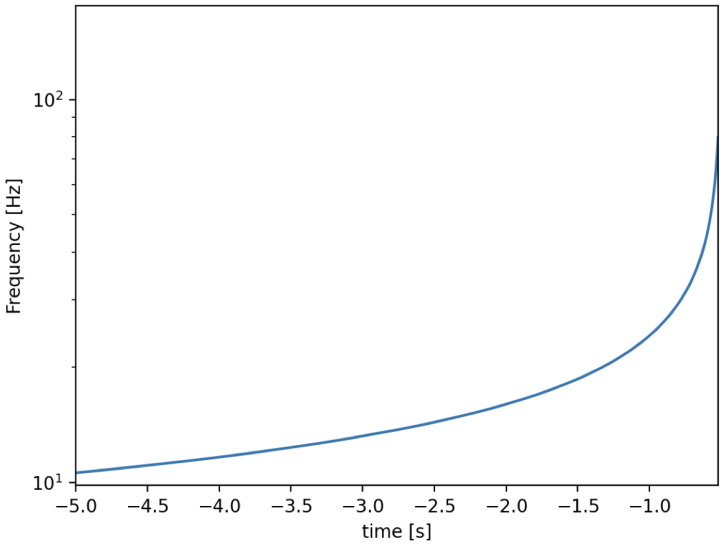

Figure 2.1: The evolution of the frequency using eq. 2.7. The frequencies increases as the objects spiral towards each other. At $t = 0$ the frequency goes to infinity and is no longer valid. This model follows the waterfall plot of fig. 2.2 well

2.2 *Comparison to Actual Data*

In order to compare data to the used model it is necessary to calculate the frequency of the measured wave. As an example the first detection of gravitational waves by LIGO will be used.
By using minima and/or maxima one can estimate the frequency f and the frequency differentiated to time $\dot{f}$ at a given point, which can be used to calculate the chirp mass using eq. 2.7 as was done in [4] who's results are given in table 2.1. The chirpmass remains somewhat constant up to the point when $\Delta t = 6.4$ ms meaning that the model seems to describe to inspiral phase quite well.

[4] M. Spurio. An introduction to astrophysical observables in gravitational wave detections. arXiv:1906.03643v1, Jul 2019

Δt (ms)	f_{gw} (Hz)	$\dot{f}_{gw}$ (Hz s^{-1})	$\mathcal{M}_z$ (kg)	$\mathcal{M}_z / M_\odot$
24.7	40	-	-	-
22.4	45	186	$6.0\times10^{+31}$	30
20.2	50	241	$5.6\times10^{+31}$	28
16.0	63	812	$7.0\times10^{+31}$	35
10.6	94	3004	$6.2\times10^{+31}$	31
6.4	156	9673	$4.1\times10^{+31}$	21
4.3	233	17746	$2.5\times10^{+31}$	12

Table 2.1: Values corresponding to fig. 2.2. The chirp mass $\mathcal{M}_z$ remains relatively stable up to the coalescence when the model used is no longer valid. This is around $\Delta t = 6.4$ ms [Spurio, 2019]

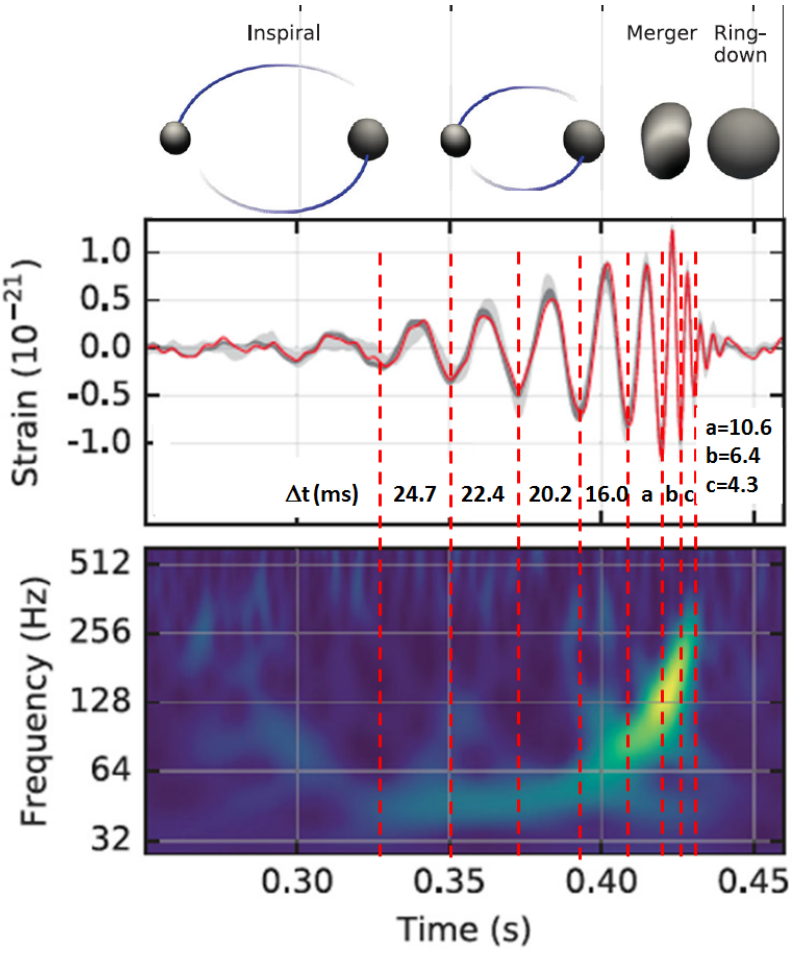

Figure 2.2: Plot of the first gravitational wave (GW150914) detection with the time difference between minima. The colour in the bottom plot (waterfall plot) corresponds to how prevalent this particular frequency was at a given point. The green/yellow curve is similar in form to the one created by the model used in this work. Taken from [Spurio, 2019]

2.3 *Coalescence*

The coalescence of a BBH or BNS event is complicated and needs to be done using numerical relativity. In this simplified model the signal goes to zero above a certain set frequency. Usually the data on coalescence is used to fine-tune the parameters obtained fitting models to the inspiral phase.
Fig. 2.3 shows an example of a wave simulated using the models discussed in this chapter. As can be seen the frequency and amplitude increase until the end of the inspiral phase.

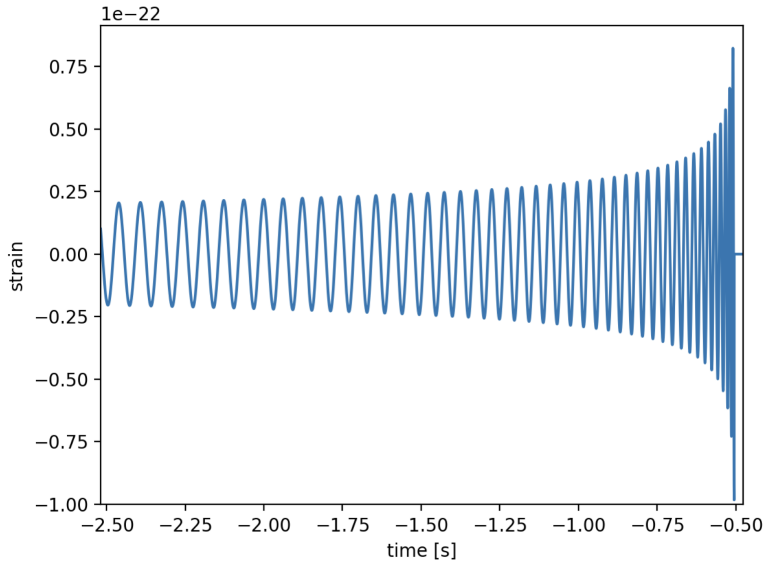

Figure 2.3: Example of a signal without noise. At $t \approx -0.5$ the objects start coalescing and we set our signal to 0.

3
Detectors

In the previous chapter the model was discussed which was used to describe the inspiral phase for binary compact objects. This was however described in an arbitrary reference frame and without any noise. In order to create realistic signals one needs functions to calculate a response s from h_+ and $h_\times$ but also as the signals are bound to be very small so it is necessary to simulate the noise the detector will produce as this will have a large effect on how precise a measurement can be.

3.1 Principle

Currently the most successful gravitational wave detectors are interferometers. These work by measuring differences in length to determine whether or not space has been warped by a gravitational wave. Using the line element (eq. 1.19) one can calculate how long it would take for light to travel a certain distance. For light the line element $ds^2 = 0$. Without loss of generality one can say that one beam of light travels in the $\hat{e}_x$ direction and one travels in the $\hat{e}_y$ direction. This can be rotated into other coordinate systems [1] For light travelling in $\hat{e}_x$ direction (thus $dy = dz = 0$) the coordinate speed is given by

[1] See section 3.5 for more information

$$\frac{dx}{dt} = \frac{1}{\sqrt{1 + h_+(t)}} \tag{3.1}$$

The coordinate speed can be higher or lower than one. The time it will take a photon to go from the origin to the end of the detector arm $L\hat{e}_x$ and back will be given by

$$T_x = \int_0^L dx\sqrt{1 + h_+(t)} + \int_L^0 \sqrt{1 + h_+(t)} \approx 2L + \frac{1}{2}Lh_+ \tag{3.2}$$

Here it was presumed that $h_+ \ll 1$ and $dh_+(t)/dt \ll (2L)^{-1}$ so one can presume that $h_+(t)$ is constant during a measurement. The same

can be done for the $\hat{e}_y$ direction which yields

$$T_y \approx 2L - \frac{1}{2}Lh_+ \tag{3.3}$$

With an interferometer one can measure the difference in return times ($T_x - T_y$), however as one can see a detector would be unable to measure a $\times$-polarised wave. This can also easily be understood by looking at fig. 1.6. If the detector itself is in the middle of the circle and the arms are up and right one can see that in case of the $\times$-polarisation both arms would contract and stretch equally, therefore there would be no difference in return times. If a wave hits the detector from the side (e.g. from the $\hat{e}_x$ direction) one arm would stretch and contract and therefore would also be measurable nowadays however the measured signal would be lower.

3.2 *Einstein Telescope*

The Einstein Telescope (ET) is a planned third generation gravitational wave detector. The third generation of detectors will be far more sensitive than previous detectors. In order to achieve a higher sensitivity the length of the arms is greatly improved (from 3 km in the case of VIRGO to 10 km in the case of ET [2]). One can easily see with eq. 3.2 that if the length increases the time-difference also increases and therefore one can detect smaller signals. Also ET will use extremely cool mirrors in order to reduce noise and use two detectors in each corner. This will make it possible to use a detector for low frequencies and one for high frequencies. Lastly ET [3] is planned to be triangular. As can be seen in fig. 3.2.
A triangular detector has several advantages. One being that as a triangular detector consists out of three detectors all in different orientations it is less likely to be unable to measure a signal. As several detectors can share tunnels this will result in a large saving as not as many tunnels will be required to be dug. In fig. 3.3 one can see that the Einstein Telescope is more sensitive in all areas and doesn't have the same "dark spots". Another advantage of the triangular shape is that the total signal of the three detectors should add up to zero. This fact can be used to reduce noise.

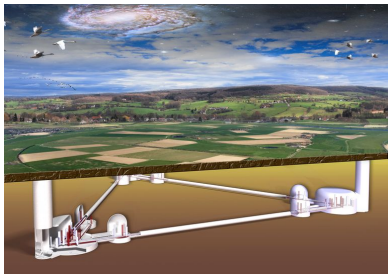

Figure 3.1: Artist's impression of the Einstein Telescope, source: Nikhef

[2] ET steering committee. ET design report update 2020. Technical report, Nov 2020

[3] Also LISA (Laser Interferometer Space Antenna) will be triangular, but be built in space. However it will take longer for LISA to be operational

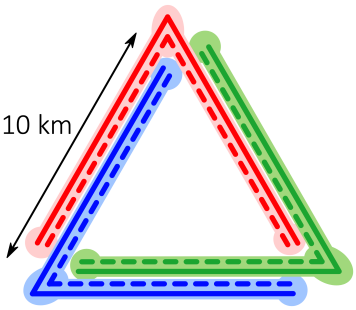

Figure 3.2: Schematic design of the Einstein Telescope, note that there are 6 detectors in total, where when combined, results from high and low frequencies will result in 3 traditional interferometers.

3.3 *Network*

Using only ET there will be several ways to determine where a signal came from. As ET is far more sensitive in low frequencies as for instance advanced LIGO or VIRGO[4] it will be possible to detect gravitational waves very early, where the movement of the

[4] LIGO and VIRGO are current detectors. LIGO is situated in the USA in Livingston and Hanford. VIRGO is situated in Italy near PISA. These detectors were used to measure the first signals

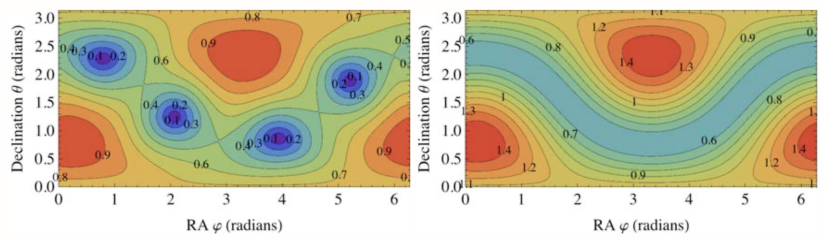

Figure 3.3: Sensitivity plots for VIRGO on the left and ET on the right (assuming ET would be built on the same location as VIRGO). Values correspond to antenna pattern functions (see 3.5 for definitions). $F = \sqrt{F_+ + F_\times}$, for ET the combined antenna pattern function is defined as $F_{tot} = \sqrt{\sum_{i=1}^{N_{det}} F_i}$. Notice that ET is less sensitive in the same areas however it is still more sensitive. Due to the triangular shape. Taken from [ET steering committee, 2020]

earth will vary significantly in order to determine where the source of this event was. This will mean that a lot of data will need to be processed and will need more computing power than was available for this work. It will also be possible to constrain parameters using the Einstein Telescope alone using shorter signals, however this will give 8 possible directions for a given signal.[5] Therefore a network of several detectors is used, where the direction can be determined in part by the time it takes a wave to travel from one detector to another. Multiple detectors will also allow for more precise measurements[6].

Detector	λ (°)	ϕ_r (°)	γ (°)	ξ (°)
ET	50.72	-5.46	0/120/240	60
CE	46.45	119.41	171.8	90
K1	36.42	-137.31	73.3	90
LI	19.61	-77.03	0	90
H1	46.45	119.41	171.8	90
L1	30.56	90.77	243.0	90

Table 3.1: The locations of detectors considered. For this work it was presumed that ET will be built between Maastricht and Aachen and that Cosmic Explorer will be built at the location of the current Hanford detector. The location for L1 and H1 were taken from [Allen, 1996] The LIGO India detector will be built in the Hingoli District, for more information see ligo-india.in

For this work it was presumed that Einstein Telescope (ET) and Cosmic Explorer (CE) [7] will eventually phase out VIRGO and LIGO, and that ET will be built between Aachen and Maastricht. Other locations such as Sardinia and Sachsen are however still in contention.[8] [9] It was also presumed that Cosmic Explorer will be built on the current Hanford site. LIGO India (LI) will be built in the Hingoli District[10].and as no power spectral density had been found for LIGO India the power spectral density of Advanced LIGO has been used to create noise. In this network KAGRA is the only detector that is currently operational.

3.4 *Noise*

As mentioned earlier the signals are presumed to be very small, so noise will have a major influence on the precision with which gravitational waves can be measured. Noise is created by many factors

[5] For more information see [Singh and Bulik, 2020]

[6] W. Del Pozzo. Inference of the cosmological parameters from gravitational waves: application to second generation interferometers Inference of the cosmological parameters from gravitational waves: application to second generation interferometers. Arxiv:1108.1317v3, Aug 2012

[7] Cosmic Explorer is the planned third generation gravitational wave detector to be built in the USA

[8] ET steering committee. ET design report update 2020. Technical report, Nov 2020

[9] International Conference ET Community 2021

[10] See ligo-india.in for more information

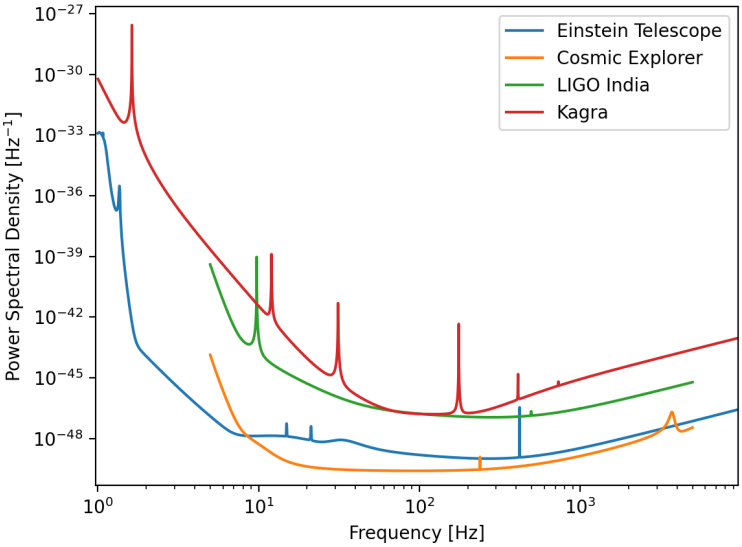

Figure 3.4: Power spectral density functions of detectors in the network that was used. A lower PSD corresponds to less noise. The Einstein Telescope and Cosmic Explorer are a big step forward compared to LIGO and KAGRA

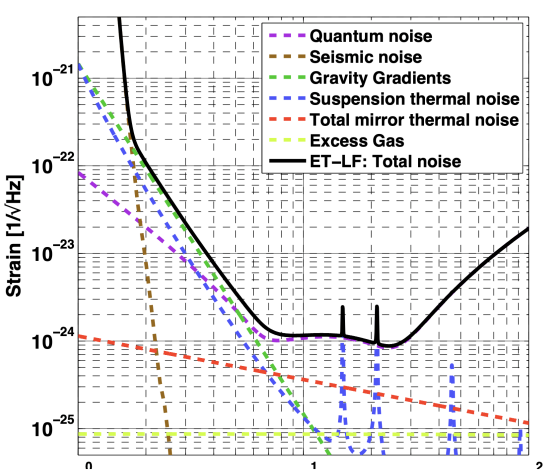

(a) Noise contributions of the low frequency detector.

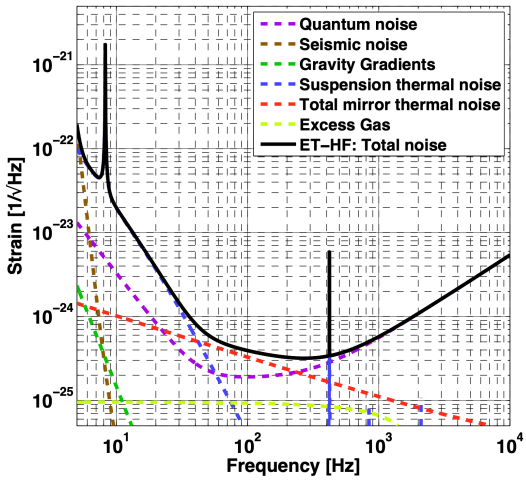

(b) Noise contributions of the high frequency detector.

Figure 3.5: How much specific sources of noise contribute to the total amplitude spectral density. As there are two detectors (one for high and one for low frequencies) there are two spectrums. Later these are combined. [ET steering committee, 2020]

such as the actual detectors but also the environment. To simulate the noise of a detector one can use the power spectral density of said detector, which can be seen in fig 3.4. A lower power spectral density will result in less noise. In fig. 3.5 the contributions of several noise sources are shown for both the low frequency and high frequency detectors of ET. To create noise a set of random numbers is generated in time space that follow a normal distribution with mean 0 and standard deviation 1. This set is then Fourier transformed and multiplied with the square root of the power spectral density (thus giving us the amplitude spectral density). In fig. 3.6 an example is shown in frequency space for ET. The orange line shows the Power spectral density whereas the blue line shows the Fourier spectrum of the noise squared.

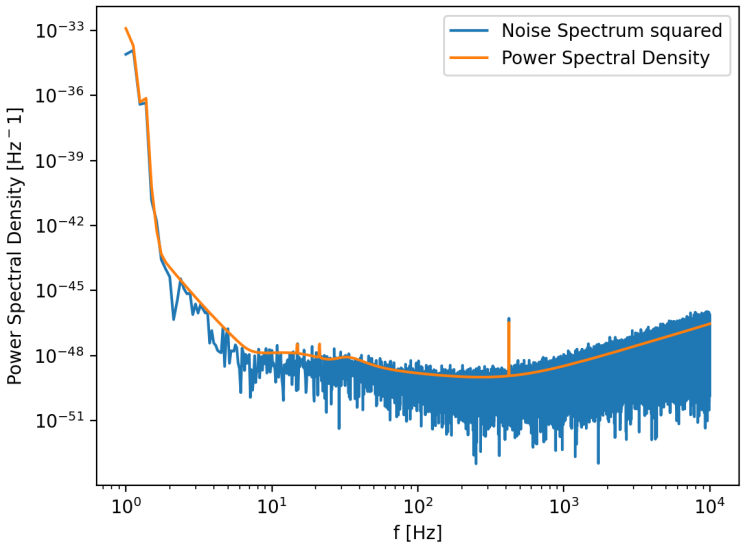

Figure 3.6: Fourier transformed squared representation of the noise of the ET detector (blue) and the corresponding power spectral density (orange).

This will then be transformed back into time space giving us realistic noise. In fig. 3.7 one can see the resulting noise in time space.
In fig. 3.7 (a) the noise is dominated by a single peak in the PSD. This should not influence our analysis later, however it becomes impossible to visually identify a signal. The best way to counteract this is to apply a filter to the total signal. A simple band pass filter was chosen where we multiplied the following function to our total signal in frequency space:

$$\frac{1}{2}\,\mathrm{erf}\left(\frac{f - f_{min}}{\sigma_f}\right) + \frac{1}{2}\,\mathrm{erf}\left(\frac{f_{max} - f}{\sigma_f}\right) \tag{3.4}$$

This gives us a band filter where the edges are "smeared out", The

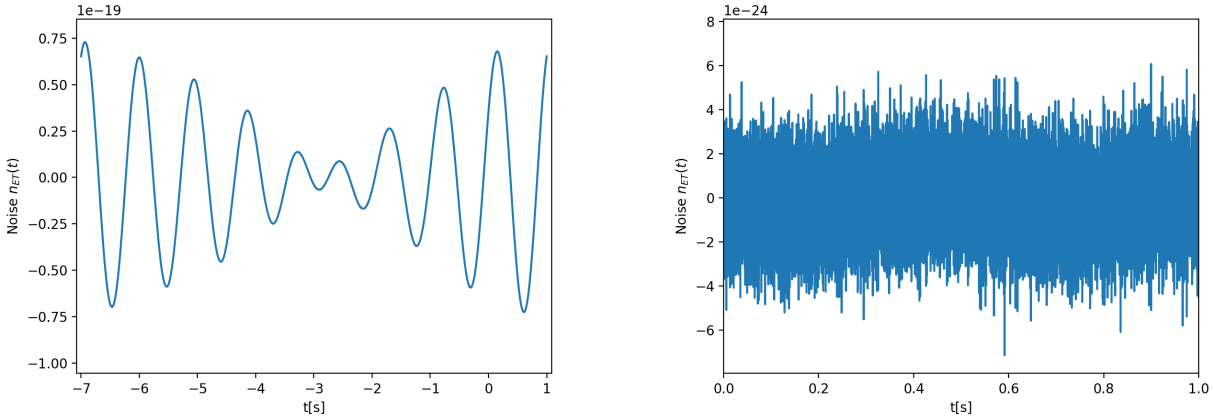

(a) Noise generated using the full power spectral density. The large peak in the PSD around $f = 1$ Hz dominates the spectral density

(b) Noise generated using the PSD but applying a high-pass filter. There is still some periodicity left, however the total amplitude is a factor of 10^4 lower.

Figure 3.7: Generated noise with and without a filter for the Einstein Telescope

parameter σ_f determines how much this is smeared out, however this filter does not have a significant influence on later results. Mostly only lower limits were chosen. For ET $f_{min} = 1.7$ Hz was chosen so the peak in low frequencies which can be seen in fig. 3.4 is not included in the noise spectrum.

3.5 *Coordinates*

Chapter 2 and section 3.1 have discussed gravitational waves travelling in the $\hat{e}_z$ direction and detectors in the $x - y$ plane. This is however not very convenient as waves will be detected from random directions and the network detectors is built on a spherical surface (earth). This means a coordinate transformation is necessary. This is done equivalently to [11], A mistake was discovered in these formulae,[12] [13] [14]. The corrected versions will be used. The signal is calculated using the beam pattern functions $F_{+/\times}(t)$ these are given by

$$F_+(t) = |\sin\zeta\,[a(t)\cos(2\psi) + b(t)\sin(2\psi)]| \tag{3.5a}$$
$$F_\times(t) = |\sin\zeta\,[b(t)\cos(2\psi) - a(t)\sin(2\psi)]| \tag{3.5b}$$

[11] Piotr Jaranowski, Andrzej Królak, and Bernard F. Schutz. Data analysis of gravitational-wave signals from spinning neutron stars: The signal and its detection. *Physical Review D*, 58(6), Aug 1998. DOI: 10.1103/PhysRevD.58.063001

[12] Instead of a factor $2\gamma + 2\zeta$ only 2γ was given in [Jaranowski et al., 1998]

[13] Jonas Hellrung. Lokalisierung von kollidierenden neutronensternen mit dem einstein-teleskop. Master's thesis, RWTH-Aachen, Jul 2020. URL https://www.institut3b.physik.rwth-aachen.de/cms/ParticlePhysics3B/Forschung/Einstein-Telekop/~jabyq/Fertige-Abschlussarbeiten/lidx/1/

[14] Timo Butz. Lokalisierung von Gravitationswellensignalen durch Zeit- & Amplitudeninformation mit dem Einstein-Teleskop. Master's thesis, RWTH-Aachen, Jul 2020. URL https://www.institut3b.physik.rwth-aachen.de/cms/ParticlePhysics3B/Forschung/Einstein-Telekop/~jabyq/Fertige-Abschlussarbeiten/lidx/1/

with

$$
\begin{aligned}
a(t) = \quad & \frac{1}{16}\sin(2\gamma+2\zeta)(3-\cos(2\lambda))(3-\cos(2\delta))\cos[2(\alpha-\phi_r-\Omega_r t)] \\
& -\frac{1}{4}\cos(2\gamma+2\zeta)\sin(\lambda)(3-\cos(2\delta))\sin[2(\alpha-\phi_r-\Omega_r t)] \\
& +\frac{1}{4}\sin(2\gamma+2\zeta)\sin(2\lambda)\sin(2\delta)\cos[\alpha-\phi_r-\Omega_r t] \\
& -\frac{1}{2}\cos(2\gamma+2\zeta)\cos(\lambda)\sin(2\delta)\sin[\alpha-\phi_r-\Omega_r t] \\
& +\frac{3}{4}\sin(2\gamma+2\zeta)\cos^2(\lambda)\cos^2(\delta)
\end{aligned}
\tag{3.6}
$$

$$
\begin{aligned}
b(t) = \quad & \cos(2\gamma+2\zeta)\sin(\lambda)\sin(\delta)\cos[2(\alpha-\phi_r-\Omega_r t)] \\
& +\frac{1}{4}\sin(2\gamma+2\zeta)(3-\cos(2\lambda))\sin(\delta)\sin[2(\alpha-\phi_r-\Omega_r t)] \\
& +\cos(2\gamma+2\zeta)\cos(\lambda)\cos(\delta)\cos[\alpha-\phi_r-\Omega_r t] \\
& +\frac{1}{2}\sin(2\gamma+2\zeta)\sin(2\lambda)\cos(\delta)\sin[\alpha-\phi_r-\Omega_r t]
\end{aligned}
\tag{3.7}
$$

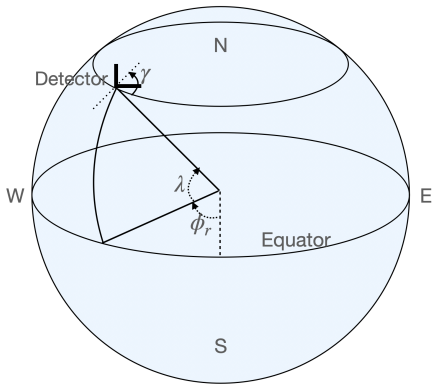

(a) The angles that have to do with the location of the detector on earth. λ is the latitude, ϕ_r is the longitude west and γ is the angle from east to the bisector between the legs of the detector.

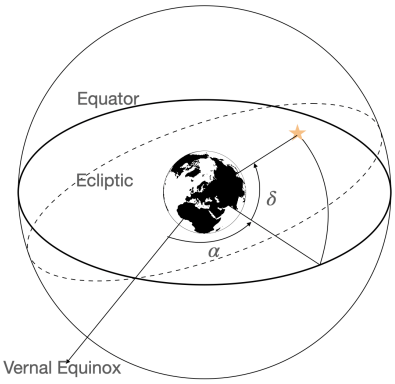

(b) Right ascension α is the angle between the vernal equinox and the projection of the point of origin in the equatorial plane, the right ascension δ is the smallest angle between the equatorial plane and the point of origin.

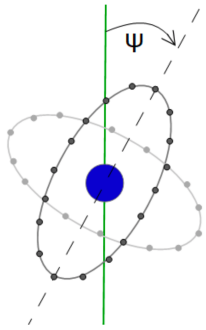

(c) The polarisation angle ψ of the GW [Hellrung, 2020]

Figure 3.8: The angles used to convert from an arbitrary frame to the detectors frame of reference.

The angles are shown in fig. 3.8. The angles α, δ and ψ determine the orientation of the wave in respect to the celestial sphere. The angles λ, ϕ_r, and γ determine where on earth the detector is positioned. Ω_r is the earth's rotational angular velocity and $\phi_r + \Omega_r t$ is the local sidereal time. Using the beam pattern functions one can calculate the signal as

$$h(t) = F_+(t)h_+(t) + F_\times(t)h_\times(t). \tag{3.8}$$

Using the model for the signal, the noise for a detector and the beam

pattern function one can generate a signal for a detector. In fig. 3.9 the same signal was generated for both one detector of the Einstein Telescope and the KAGRA detector.

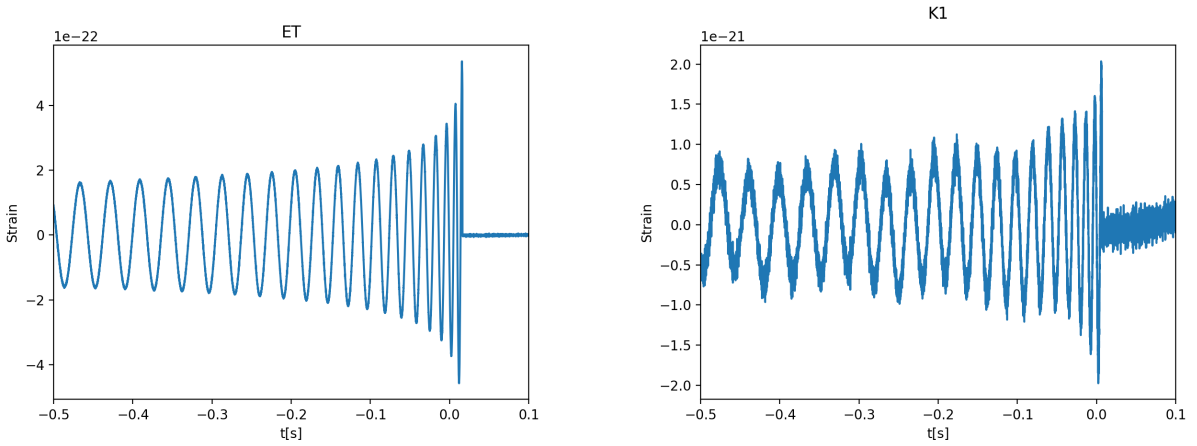

(a) Signal measured by Einstein Telescope. A filter was applied with $f_{min} = 1.7$ Hz

(b) Signal measured by KAGRA. No filter was applied in this case, this might have interfered with the signal

Figure 3.9: Simulated signals for the same BBH event with noise for ET and KAGRA,.Despite a worse orientation (and henceforth smaller amplitude) ET has a better signal to noise ratio. $\mathcal{M}_z = 26M_\odot$, $D_L = 224$Mpc

4
Method

Once one has detected a gravitational wave one wishes to understand which objects have created said wave. In order to do this it is necessary to fit the previously described model to the measured data, however the model has a high dimensionality. Also by simply reducing the PSD to a standard deviation one loses information about the frequency dependence of the noise. This calls for a different strategy than for instance the least squares method. One method currently often used in astronomy is the Nested Sampling Algorithm by J. Skilling [1]. The following chapter will explain how this method works and how it is implemented.

[1] J. Skilling. Nested sampling for general Bayesian computation. *Bayesian Analysis*, (4):833 – 859, Dec 2006. DOI: 10.1214/06-BA127

4.1 Nested Sampling

Nested Sampling is an algorithm to create posterior distributions in order to infer parameters from a signal under the assumption that a certain model is correct. It can also be used for comparing models.

Bayes' Theorem

Nested Sampling is based on Bayes' Theorem, which states that

$$P(A \mid B) = \frac{P(B \mid A)P(A)}{P(B)} \tag{4.1}$$

where $P(B) \neq 0$. $P(A \mid B)$ means the probability of A happening if B is given. This can be used to calculate the probability of certain parameters specific to the gravitational wave $\vec{\theta}$ and cosmological parameters $\vec{\Omega}$ given a measurement D and a model M[2]. This means eq. 4.1 can be written as

[2] To calculate the distance from a source the ΛCDM model is used and the model described in chapter 2 is used for the fitting

$$P(\vec{\theta}, \vec{\Omega} \mid D, M) = \frac{P(D \mid M, \vec{\theta}, \vec{\Omega})P(\vec{\theta}, \vec{\Omega})}{P(D \mid M)} = \frac{L(\vec{\theta})\pi(\vec{\theta})}{Z} \tag{4.2}$$

where $L(\vec{\theta})$ is called the likelihood, $\pi(\vec{\theta})$ is called the prior and Z is called the evidence.

Likelihood: $L(\vec{\theta})$

The likelihood is the probability of measuring data D given a certain model M and parameters $\vec{\theta}, \vec{\Omega}$. The total likelihood is the product of the likelihood of all the detectors[3]:

$$L(\vec{\theta}) = P(D \mid \vec{\theta}, \vec{\Omega}, M) = \prod_{k=1}^{N_{det}} P(D^{(k)} \mid \vec{\theta}, \vec{\Omega}, M). \tag{4.3}$$

[3] Assuming that all detectors work independent of one another

The likelihood for a certain detector is given by [4]

$$P(D^{(k)} \mid \vec{\theta}, \vec{\Omega}, M) = \exp((s^{(k)} - h^{(k)}(\vec{\theta}, \vec{\Omega}) \mid s^{(k)} - h^{(k)}(\vec{\theta}, \vec{\Omega}))/2) \tag{4.4}$$

[4] Lee S. Finn. Detection, measurement, and gravitational radiation. *Phys. Rev. D*, 46:5236–5249, Dec 1992. DOI: 10.1103/PhysRevD.46.5236

The measured strain is given by $s^{(k)}$, the theoretical strain (which is calculated using the model and various parameters) is given by $h^{(k)}(\vec{\theta}, \vec{\Omega})$. In eq. 4.4 the following notation is used:

$$(\mathrm{f} \mid \mathrm{g}) := \int_0^\infty df \frac{\tilde{\mathrm{f}}^* \tilde{\mathrm{g}} + \tilde{\mathrm{f}} \tilde{\mathrm{g}}^*}{S_n(f)}. \tag{4.5}$$

As the signal-to-noise ratio is given as [5]

$$\rho^2 = (h(f) \mid h(f)) \tag{4.6}$$

[5] C. J. Moore, R. H. Cole, and C. P. L. Berry. Gravitational-wave sensitivity curves. *Classical and Quantum Gravity*, Dec 2014. DOI: 10.1088/0264-9381/32/1/015014

The likelihood is the exponential of minus the signal- to-noise ratio of the residual.

Prior: $\pi(\vec{\theta})$

The prior is the probability that a parameter has a certain value. Mostly these are taken to be uniform between two limits. If the prior is chosen very small this will have an effect on the uncertainty as one would expect a standard deviation of $\sigma = (b-a)/\sqrt{12}$ for uniform samples[6].

[6] a,b are the limits of the uniform distribution

Evidence: Z

The main goal of Nested Sampling is to calculate the evidence Z, which is the probability of measuring D if model M is given irrespective of the parameters. This means this can be calculated by integrating over prior-space:

$$\begin{aligned} Z = P(D \mid M) &= \iint d\vec{\theta} d\vec{\Omega} P(D \mid \vec{\theta}, \vec{\Omega}, M) P(\vec{\theta}) P(\vec{\Omega}) \\ &= \int d\vec{\theta}' L(\vec{\theta}') \pi(\vec{\theta}') \end{aligned} \tag{4.7}$$

$\vec{\theta}$ is a vector containing the parameters of the GW and $\vec{\Omega}$ are the cosmological parameters. In order to reduce the dimensionality of the integral one introduces the parameter X which is defined as

$$X(\lambda) = \int_{L(\vec{\theta})>\lambda} d\vec{\theta}\pi(\vec{\theta}) \tag{4.8}$$

This is similar to integrating over the radius in spherical coordinates and this parameter can be thought of as the percentage of the prior-space which has a higher likelihood than the current point. Using this eq 4.7 can be written as

$$Z = \int_0^1 dXL(X) \tag{4.9}$$

This integral was calculated using the Monte Carlo method. To do so one starts of with N_{live} live points, which are randomly chosen in the total parameter-space $\vec{\theta}' = \vec{\theta} \cup \vec{\Omega}$. Then the worst live point is added to the samples and replaces the old point with a new one which has a higher likelihood than the previous point, therefore a smaller X. The issue however is that it is not possible to know exactly what the value X_i is of the i-th sample. There is however a noisy estimator which estimates that the X value corresponding to the i-th sample is

$$\langle X_i \rangle = \exp(-i/N_{live}). \tag{4.10}$$

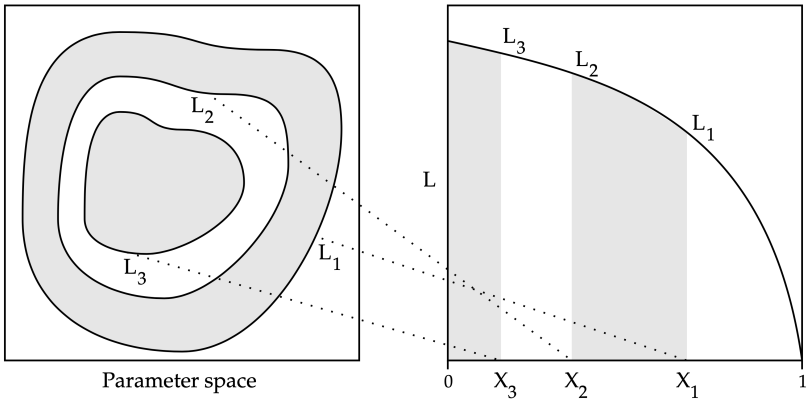

Figure 4.1: Figure showing Nested Sampling, starting with N_{live} live points the point with the worst likelihood is picked. This is the first sample (in this case L_1). This point is then replaced by a new point with a higher likelihood, so it must be in the marked area. Then the point with the worst likelihood is picked as the second sample with likelihood L_2 and this point has an X appointed to it which can be calculated using eq. 4.10.[Skilling, 2006]

Using the likelihood for the calculated samples and an estimate for X it is possible to get an approximation for Z (eq 4.9)

$$Z = \int_0^1 dXL(X) \approx \sum_{i=1}^{N_{Sampl}} (X_i - X_{i-1}) \cdot \frac{(L_i + L_{i-1})}{2} = \sum_{i=1}^{N_{Sampl}} w_i \tag{4.11}$$

where w_i is called the importance weight. As can be seen in fig. 4.2, the very first values with very low likelihood are not important to

the calculation of Z as their likelihood is too small, however also the samples with very high likelihood don't contribute as much as the volume X has become too small for dX to make a contribution to Z.

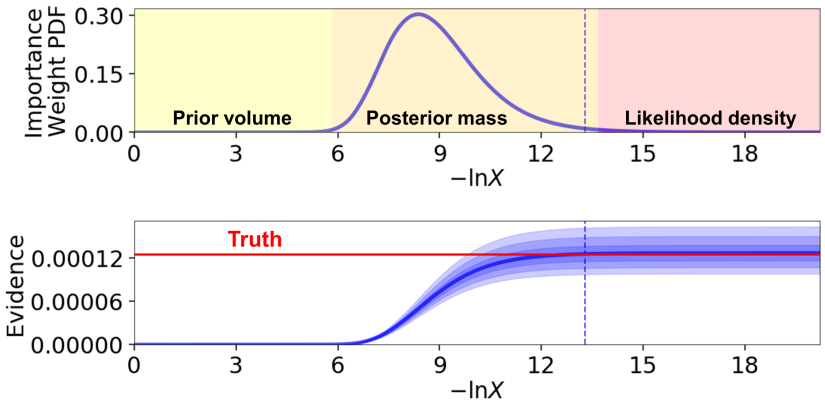

Figure 4.2: Calculation of Z and weight $w(X)$ dependant on the volume X. It can be seen that if the likelihood is very low and the volume X is large that a sample will not contribute a lot to the evidence Z. Neither will a sample contribute much if the likelihood is high and the volume is too small. Example taken from [Speagle, 2020]

Choosing New Points

Once the point of worst likelihood has been added to the samples it has to be replaced with a new point. A point is picked in the unit cube $\vec{u}$ and transformed to the prior space. However as the volume X with a likelihood better than the current likelihood shrinks exponentially this gets very inefficient very fast, so another method of finding new points is needed.

Box The easiest solution would be to draw an n-dimensional box around the live points and leave some extra space so points can migrate. However this method does not take into account any possible correlations and if points move into a local and absolute minimum a box will be drawn around the entire area which makes it very inefficient.

Ellipses A far more efficient method is by using ellipses. The algorithm used is based on the algorithm used by Dynesty [7]. The basic idea is to draw a certain number of ellipses around the live points and pick a new point within this ellipse. This is more efficient in part due to the fact that this method also takes correlations into account and multiple ellipses are drawn around points that have "grouped" together To start, one calculates the covariance matrix of the live points C. This is multiplied with a factor of $n_{dim} + 2$[8]. To calculate whether or not a point is within an ellipse the distance is calculated

[7] Joshua S Speagle. dynesty: a dynamic nested sampling package for estimating Bayesian posteriors and evidences. *Monthly Notices of the Royal Astronomical Society*, 493(3):3132–3158, Feb 2020. DOI: 10.1093/mnras/staa278

[8] For more information see [Meckes].

which is defined as

$$d = (\vec{u} - \vec{a})^T \cdot C^{-1} \cdot (\vec{u} - \vec{a}), \tag{4.12}$$

where $\vec{u}$ is the point within the unit cube and $\vec{a}$ is the center of the ellipse (which corresponds to the mean vector of the points used. The covariance matrix is then multiplied with the largest distance d, so henceforth if a distance is calculated it is outside of the ellipse if $d > 1$.[9]

[9] Usually the factor $n_{dim} + 2$ is not enough to enclose all points, therefore it is not very important as this process will dominate the volume.

Choosing New Points The goal is to choose a point $\vec{v}$ uniformly from an ellipse, to do this one picks a point from a unit sphere. This is accomplished by chosing n_{dim} numbers which are normally distributed around 0 with standard deviation $\sigma = 1$. These are the elements of the vector $\vec{v}$. Then this vector is normalised so $|\vec{v}| = 1$. This gives a point on the surface of the unit sphere. Then a radius is picked by taking the n_{dim}-th root of a random number between 0 and 1. If this radius is multiplied with the previously chosen direction one gets a new point within the unit sphere. To transform this point from the unit sphere into the ellipse the vector $\vec{v}$ is multiplied with the lower Cholesky decomposition of the covariance matrix C. To compensate for the offset of the ellipse $\vec{a}$ is added. This gives a random point within the ellipse.

Creating Multiple Ellipses If one has a local and an absolute minimum in the likelihood landscape it will be possible that points converge to both minima until all points near a minimum have been replaced. In this case there would be a lot of prior space where points will be generated that are no longer in the volume X as these likelihoods are not good enough. It is then easier to draw multiple ellipses. To create an ellipse one needs a minimum of $2n_{dim}$ points (if one doesn't have enough points one could have a plane instead of an ellipse.) If one has more then $4n_{dim}$ points it is possible to create two instead of one ellipse. To do this two clusters are created with as little overlap as possible and create two bounding ellipses around these points. The algorithm used to create these clusters is the KD cluster algorithm [10]. If the sum of the new volumes

[10] For more information on the KD cluster see appendix A

$$V_1 + V_2 < \lambda V_{orig} \tag{4.13}$$

the splitting of the ellipses is accepted and one tries again until either there are not enough points to split into more ellipses or eq. 4.13 is not fulfilled. $\lambda = 0.5$ was chosen as was used in Dynesty. In tests with $\lambda = 0.7$ the program seems to run less stable and more likely to run into a local minimum.

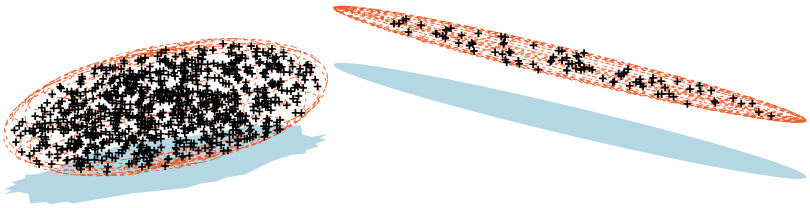

Figure 4.3: Example of multiple ellipses in 3D where all points are clustered in two ellipses. Drawing one large ellipse around all points would result in a much larger volume, therefore it is far more efficient to draw two smaller ellipses around these clusters. Taken from [Feroz et al., 2009]

Random Walk

In the original paper by Skilling [11] a random walk algorithm was used. Instead of picking a random point a live point is copied which already fulfils the requirement that the likelihood has to be better than the likelihood of the "killed" point. Starting from this point one does a random walk where every step is accepted as long as this new point has a likelihood higher than the point that is to be replaced.

[11] J. Skilling. Nested sampling for general Bayesian computation. *Bayesian Analysis*, (4):833 – 859, Dec 2006. DOI: 10.1214/06-BA127

Stopping Criterion

Naturally at some point the analysis must stop. Therefore a stopping criterion is required. If one were to choose a certain amount of samples one would run into the issue that signals with a high signal-to-noise ratio need more samples to ascertain good results as can be seen in fig. 4.4.

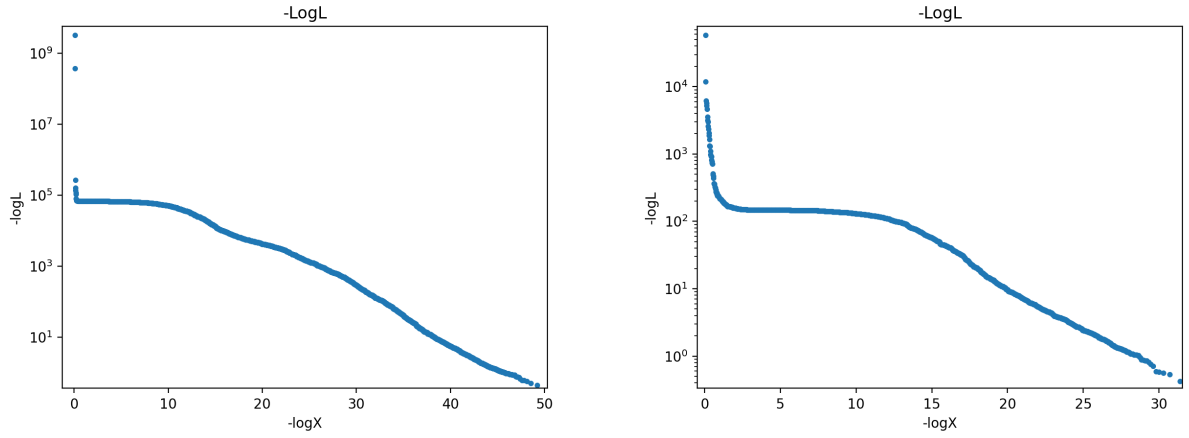

(a) $z = 0.050$, $\mathcal{M}_z = 26M_\odot$

(b) $z = 0.51$, $\mathcal{M}_z = 11M_\odot$

Figure 4.4: Two evolutions of the $\log L$. After $\log X \approx -10$ the behaviour is quasi-linear. Note that the likelihoods for fig. 4.4 (a) are higher than for fig. 4.4 (b) as this event was closer despite the higher $\mathcal{M}_z$

Using the $\log L$ might also not work as it is not always known beforehand what an acceptable likelihood might be. The best way is to estimate how much of the evidence Z has not been integrated over

yet

$$Z_{remain} = \int_0^{X_{remain}} dX' L(X') \leq X_{remain} \cdot \max(L). \tag{4.14}$$

Using eq. 4.14 and the estimate for Z one calculates how much evidence is left. The criterion $Z_{remain}/Z < 0.1$ was chosen. Once this criterion has been fulfilled one proceeds to the next step, adding the live points.

Adding Live Points

Once one is certain enough of the parameter space has been scanned to give a reliable estimate of Z, there will still be N_{live} live points with the best likelihoods left. These can also be used to calculate Z and are very important for the construction of the posterior likelihood. However as no more new live points are being created once a live point was added to the samples there is a varying number of live points and therefor the previous estimate for X (eq 4.10) can not be used. The estimate used in this case is

$$X_i = X_{final} \cdot \left(1 - \frac{i+1}{N_{live}+1}\right) \tag{4.15}$$

where X_{final} is the volume corresponding to the last sample

4.2 *Approximating Posterior Distribution*

Now using the samples and the evidence Z, one wishes to use these to approximate the posterior distribution. In order to do this one has to assign every sample a weight so samples created early with very bad likelihoods don't contribute as much to the posterior distribution as samples that have been proposed later on and therefore have a better likelihood. The weight of a sample is given by w_i/Z where w_i was defined in eq. 4.11. These weights can also be used to easily calculate the mean value for a parameter as

$$\bar{x} = \sum_{i=1}^{N_{samples}} \frac{w_i}{Z} x_i \tag{4.16}$$

One can also calculate the standard deviation as $\sigma_x = \bar{x^2} - \bar{x}^2$. Sometimes however the posterior distribution cannot be described properly by a Gaussian distribution. In this case one can calculate confidence intervals with an algorithm somewhat similar to the Feldman Cousins [12] algorithm, the samples are sorted by descending likelihood and sum the normalised weights of the samples[13] until the desired interval is reached and pick the maximum and minimum value of the accepted samples to create a confidence interval.

[12] Gary J. Feldman and Robert D. Cousins. A Unified Approach to the Classical Statistical Analysis of Small Signals. *Physical Review D*, 57(7):3873–3889, Apr 1998. DOI: 10.1103/PhysRevD.57.3873

[13] The normalised weight of a sample is given by w_i/Z

4.3 *Runtime and Stability*

In this chapter the amount of live points and methods of picking new points have been discussed. Both have an influence on the runtime. As the log volume scales as $\log X \sim {N_{live}}^{-1}$ the amount of samples needed to achieve the same $\log X$ is proportional to N_{live}, however it seems like the runtime doesn't increase linearly as the average amount of tries necessary also increases. More N_{live} per dimension however does mean that it is less likely not to find the actual minimum. it can be challenging to detect for cases with very low amplitudes if the actual minimum was found. In other cases it can often be seen in a log X - log L plot as seen in fig. 4.5. In this figure the slope decreases in the end and the program stops at a high log L. Lastly important to the runtime is the fact that the

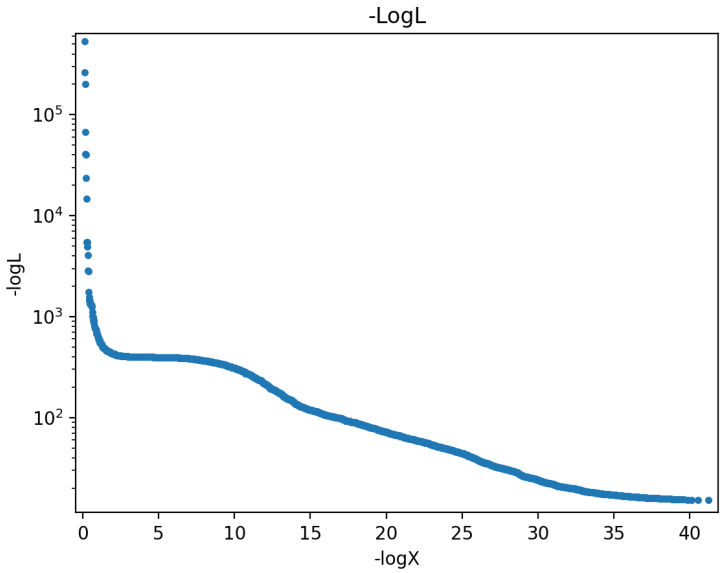

Figure 4.5: In this figure one sees the evolution of an analysis where the actual parameters weren't found unlike in fig. 4.4 the slope decreases in the end and the program ends at a low (i.e. bad) likelihood.

amount of tries necessary before a new point is accepted increases exponentially as can be seen in fig. 4.6. Therefore a limit is set and if no new point has been found before this limit is reached, the random walk algorithm is used instead of using ellipses.

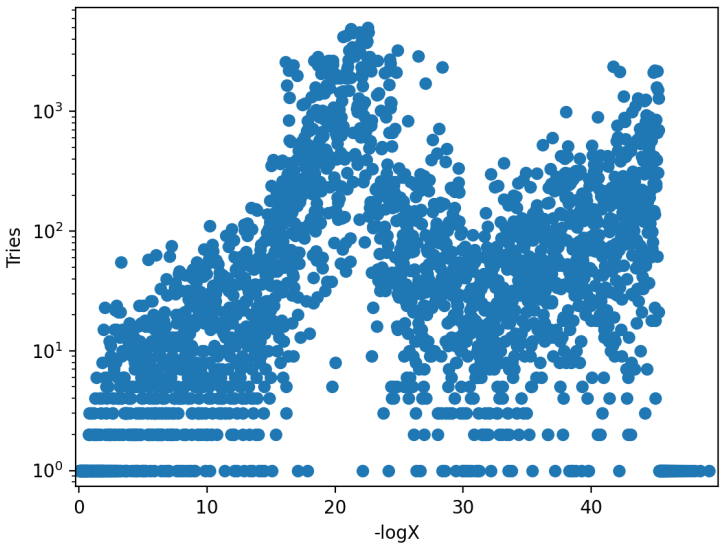

Figure 4.6: The number of attempts required to find a new point compared to the log volume. Note how the number of tries increases exponentially, however if certain values have converged the volume of the ellipses decreases strongly and the number of attempts follows suit.

5
Analysis

With the means to simulate and analyse the detection of gravitational waves, this chapter will discuss the results obtained. This chapter consists out of three parts, the first will discuss the settings of the analysis. The second part will discuss how well our program could infer the parameters of a gravitational wave. The last part will discuss how one can determine cosmological parameters and how well this can be done with this method.

5.1 Settings and Peculiarities Concerning the Analysis

Before discussing the results of the analysis this section will explain what settings were used for the nested sampling algorithm. Starting with the number of live points, $N_{live} = 50$ was chosen as this gave the results wanted and seemed stable enough. More live points would have resulted in the program running better (i.e. a smaller chance of running into a local minimum of the likelihood), but would have resulted in longer running times to achieve the same log X and therefore also longer for the same evidence Z [1]. In order to generate points within the prior, points were generated in an N_{dim} dimensional unit cube, after which these points were transformed to prior space. For most values this transformation was linear, however the declination δ and inclination ι were transformed on a unit sphere as $\pm\pi/2$ and $0, \pi$ are poles for the declination and inclination respectively. Therefore for the declination the following formula was used

[1] See sec. 4.3 for more information

$$\delta = \arccos(1 - 2u_\delta) - \frac{\pi}{2}, \tag{5.1}$$

where u_δ is the parameter on the unit cube. For ι the same formula was used without the $\pi/2$ factor as the declination $\delta \in [-\pi/2, \pi/2]$ and $\iota \in [0, \pi]$. All of the other parameters were sampled uniformly in the following prior spaces:

- $\alpha \in [0, 2\pi]$
- $\delta \in [-\pi/2, \pi/2]$
- $z \in [0, 1]$
- $\psi \in [0, \pi/2]$
- $\phi_c \in [0, 2\pi]$
- $h \in [0.1, 1]$
- $\Omega_m \in [0, 1]$
- $\Omega_\Lambda \in [0, 1]$

In this case ψ was not sampled from 0 to 2π as several combinations of ψ and ϕ_c can result in the same wave. The priors for $\mathcal{M}_z$ and t_c have been varied, however usually these can be determined very well so the prior doesn't influence the end results. The prior for h was chosen between 0 and 1 in order to compare results with the paper written by Del Pozzo as this covers very similar subjects[2]. This will be discuss later in sec. 5.3 in more detail. Lastly $\mathcal{M}_z$ was sampled instead of $\mathcal{M}_c$ as this removes one very strong correlation between $\mathcal{M}_c$ and z.

[2] W. Del Pozzo. Inference of the cosmological parameters from gravitational waves: application to second generation interferometers Inference of the cosmological parameters from gravitational waves: application to second generation interferometers. Arxiv:1108.1317v3, Aug 2012

5.2 *Inferring parameters*

To show the results of the analysis two events are discussed in particular. Table 5.1 details the input parameter and the results obtained.

	Run I		Run II	
	Input	Results	Input	Results
α(rad)	3.5173	3.5173 ± 0.0021	2.84	3.09 ± 0.18
δ(rad)	0.1422	0.1415 ± 0.0038	0.32	-0.11 ± 0.26
$\mathcal{M}_z(M_\odot)$	26.37113	26.37088 ± 0.00090	10.5651	10.5652 ± 0.0036
D_L(Mpc)	224	300 ± 50	2.92×10^3	$(2.96 \pm 0.94) \times 10^3$
ψ(rad)	0.56	0.75 ± 0.35	0.64	0.64 ± 0.28
ι(rad)	2.54	2.72 ± 0.15	2.01	1.93 ± 0.52
$t_c(s)$ (s)	0.011457	0.011471 ± 0.000049	-0.2077	-0.2016 ± 0.0027
ϕ_c(rad)	3.18	3.55 ± 0.70	2.94	3.07 ± 0.50

Table 5.1: The data obtained from two runs. The given standard deviation is the standard deviation of the probability distribution.

Here D_L was calculated for every sample using z, h, Ω_m and Ω_Λ, where $\mathcal{M}_z$ was sampled instead of $\mathcal{M}_\rfloor$. Better results are obtained for D_L if it is sampled directly or through one parameter (e.g. z with h fixed).

Angular Precision

It is important to localise the source of a signal. This is partly done by multilateration meaning that the time differences between when detectors measure the signal are compared. As t_c is the point in time when the wave reaches the centre of the earth and rotations influence when a specific detector detects a wave this has an influence on the

localisation of the event. In fig. 5.1 the angular precision is shown of an event.

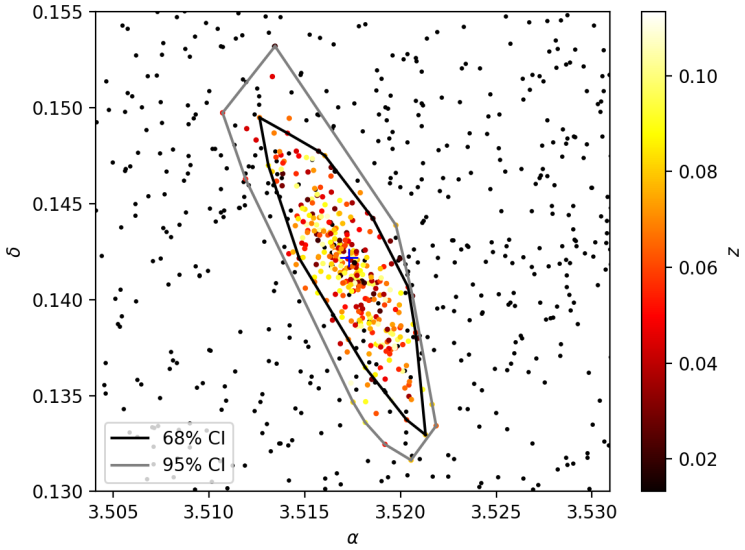

Figure 5.1: Plot showing the angular precision of an analysis. The coloured points within the grey contour have a combined weight of 90%, within the black contour the combined weight is 68%. The colour of the points denotes the redshift of the corresponding galaxy. The black points were not chosen in the 2σ area. The blue cross shows the actual location.

The black and grey contours show the 1 and 2σ areas respectively. This is calculated by summing up the weights discussed in eq. 4.11 divided by the evidence Z until the wanted confidence level is achieved. The coloured points are the points chosen in the 2σ area and the colour represents the redshift of the corresponding galaxy. In fig. 5.2 one can see that not only the luminosity distance is important to how precise one can measure the point of origin, while events with higher uncertainties have a higher luminosity distance it does not seem to be the only criterium of importance. Another contributing factor could be the analysis itself, if all points converge early on to a false minimum and only move relatively late into the actual minimum, then the spread of points with a high weight w_i will be larger, therefore the standard deviation will be larger.

Inferring Mass and Distance

As discussed in chapter 2 the amplitude depends mostly on the frequency (and therefore the redshifted chirp-mass) and the luminosity distance. As both frequency and time of coalescence can be measured precisely one can then calculate $\mathcal{M}_z$ quite precisely. $\sigma_{\mathcal{M}_z} \sim 10^{-4}\mathcal{M}_z$ Luminosity distance is more difficult to measure precisely as can be seen in fig. 5.3 When comparing our results to the latest catalogue[3] it seems the results shown in fig. 5.3 results are similar if not more

[3] R. Abbott, T. D. Abbott, S. Abraham, F. Acernese, K. Ackley, and et al. GWTC-2: Compact Binary Coalescences Observed by LIGO and Virgo during the First Half of the Third Observing Run. *Physical Review X*, 11(2), Jun 2021b. DOI: 10.1103/PhysRevX.11.021053

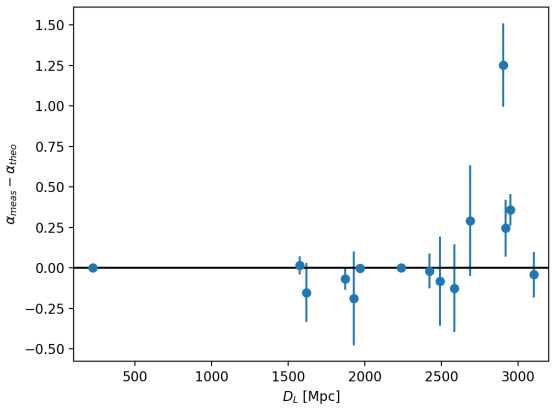

(a) The residuals for the right ascension measurements

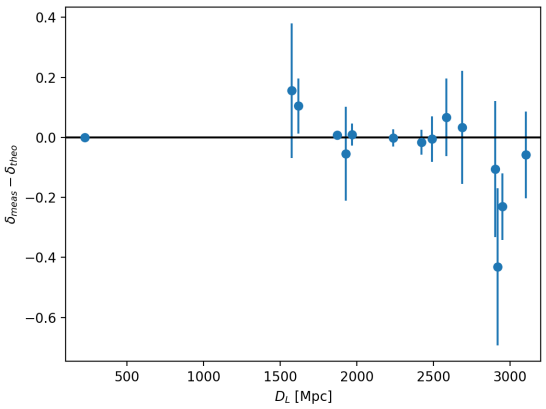

(b) The residuals for the declination measurements

Figure 5.2: The residuals for the angles for several measurements. It is clearly visible that not only the luminosity distance is of importance for a precise measurement

precise, which would be expected as the detectors used are far more precise. One major difference when comparing these results however is that the catalogue uses real data and this work uses simulated data.

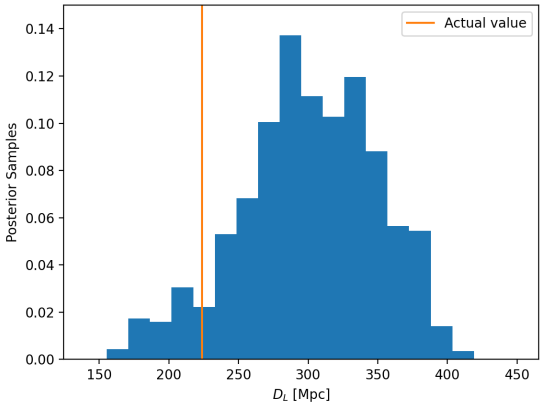

(a) Posterior samples $D_L = 300 \pm 50$ Mpc

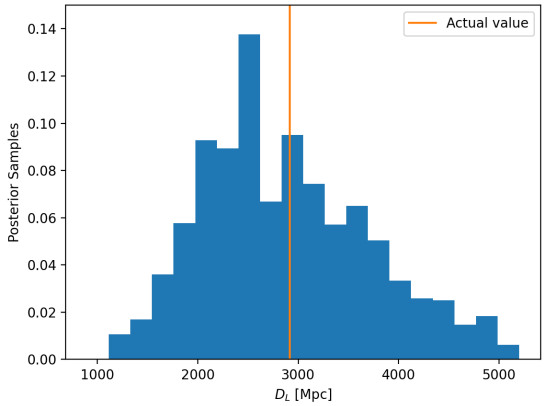

(b) Posterior samples $D_L = (2.96 \pm 0.94) \times 10^3$ Mpc

Figure 5.3: Posterior samples for the luminosity distribution. Histograms are weighted using w_i / Z

Inclination, Polarisation Angle

Lastly discussing the determination of both the polarisation angle and inclination. These parameters don't have a very large effect on the wave and are therefore more difficult to measure. As can be seen in tab. 5.1 also these parameters can be determined, be it not with huge precision.

Residuals

In fig 5.4 the residuals for event 1 have been plotted. While phase and frequency have been determined well, some ambiguity remains about the amplitude. This will be in part due to the fact that the luminosity distance has not been determined perfectly. Also the fact that we chose $Z_{rem}/Z = 0.1$ will have an influence as one would get better results if one integrates over more evidence. In Dynesty the standard value is 1%, however in Bilby which is designed for GWs and uses Dynesty as it's backend the value is 10% (like in our case). This should lead to improved residuals and improved parameters, however should have a small influence on the standard deviations as these will be determined by the posterior distribution which won't differ much.

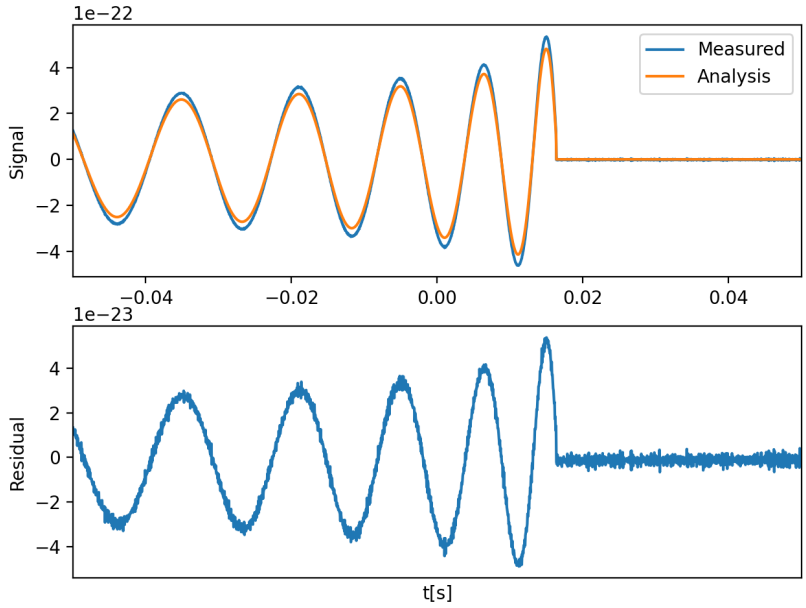

Figure 5.4: Residuals of event 1. While both phase and frequency have been determined well, the amplitude is still ambiguous. As can be seen in tab. 5.1 the luminosity distance has been overestimated for this event, leading to a smaller amplitude

5.3 *Determining Cosmological Parameters*

As previously touched upon Schutz proposed in 1986[4] that it would be possible to use standard sirens in gravitational wave astronomy as one uses standard candles in "regular" astronomy. As the luminosity distance can be inferred directly one can calculate the Hubble parameter assuming the redshift is known. There are two categories of gravitational wave events: events without an electromagnetic counterpart called dark events and events with an electromagnetic counterpart. In case one has an EM counterpart one can measure the

[4] Bernard F. Schutz. Determining the Hubble constant from gravitational wave observations. *Nature*, 323(6086):310–311, Sep 1986. DOI: 10.1038/323310a0

redshift of the EM counterpart and use this in the analysis for the GW event. In the case of dark events inferring the redshift is far more difficult.

Determining the Redshift and Hubble Parameter for Dark Events

In the case of a dark event there is no EM counterpart to the GW event. However the redshift is very important as both the redshifted chirp mass $\mathcal{M}_z$ and the luminosity distance D_L depend on the redshift, however it does not enter the model directly, therefore there are several combinations of chirp mass and Hubble parameter for the same event. In order to determine the redshift one wishes to correlate a dark siren with a galaxy catalogue. To do this the way the right ascension α, declination δ and redshift z of the samples are picked is slightly changed. First three random values for (α, δ, z) are picked. Then the kd-tree algorithm [5,6] is used to find the galaxy with the shortest distance to this point, where the distance is defined as

$$d = \sqrt{(\alpha - \alpha_{gal})^2 + (\delta - \delta_{gal})^2 + (z - z_{gal})^2} \tag{5.2}$$

Once the galaxy has been found with the smallest distance d these values are used instead of the ones generated. The luminosity distance is calculated from the redshift and the cosmological parameters h and Ω_i. Thus correlations in the galaxy database can be used to determine the redshift of the measured event. The Sloan Deeps Sky Survey Database was used up to $z = 1$. This database has a good coverage in large parts of the northern hemisphere. The fact that there are spots where coverage is weak is not important as one would use multiple or different databases if a wave originated from this direction. In fig. 5.5 the distribution of redshift is shown for galaxies in the SDSS database. Fig. 5.6 shows the (a) the weighted samples of the Hubble parameter and fig. 5.6 (b) shows the evolution of the redshift during the nested sampling algorithm. Both Ω_r and Ω_Λ did not converge for any redshift z and had standard deviations close to $1/\sqrt{12}$. These results seem quite promising however if the Hubble parameter is changed to $h = 0.3$ one gets similar results for the Hubble parameter and an overestimation on the redshift. Therefore this seems to be a characteristic of the analysis with the previously described settings. The Hubble parameter seems to converge first and afterwards the redshift converges to the correct value.
The results improve if $\mathcal{M}_c$ is sampled instead of $\mathcal{M}_z$. In this case the redshift converges before the Hubble constant, so it seams less of a characteristic of the analysis or settings. However for $h = 0.3$ the results are still not great as can be seen in fig. 5.7 (b)[7]. Comparing the results for a dark event with [Abbott et al., 2021a] one finds that

[5] Jon Louis Bentley. Multidimensional Binary Search Trees Used for Associative Searching. *Commun. ACM*, 18(9):509–517, Sep 1975. DOI: 10.1145/361002.361007

[6] The code as found on rosettacode.org was used

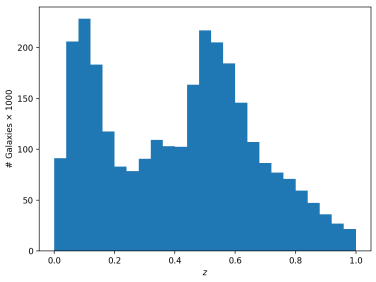

Figure 5.5: Distribution of the redshift for galaxies in the SDSS database

[7] Sampling z and $\mathcal{M}_c$ separately is very inefficient as relatively early the redshifted chirp mass converges strongly and therefor these values have to be picked within a plane. To speed up this process some values were fixed to their input values. This did not seem to have a significant effect on either h or z.

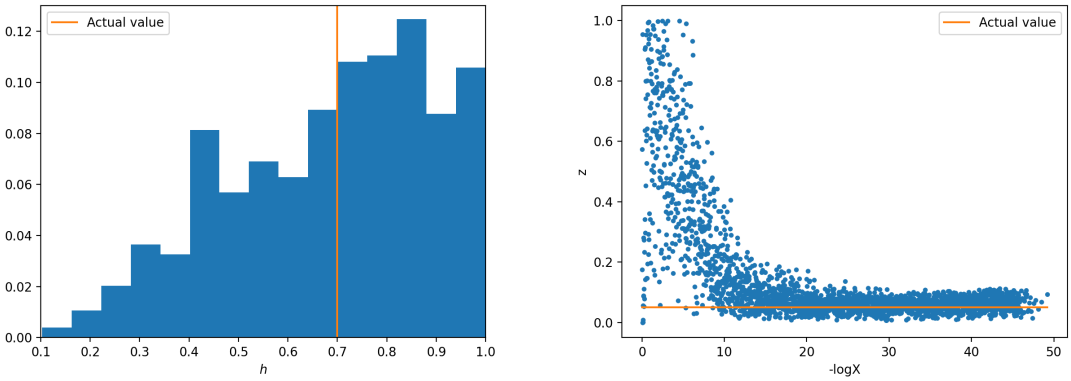

(a) Weighted samples for the Hubble parameter

(b) Evolution of redshift, the solid line is the actual value of the redshift.

Figure 5.6: Results for a dark event assuming $h = 0.7$ and redshift $z = 0.05$. Both parameters converge well, however for $h = 0.3$ we obtain similar results for the Hubble parameter and an overestimation for the redshift.

in this work the posterior distribution for the Hubble parameter was nearly uniform when using dark events, therefore it is possible the analysis in this work converged more than it should have.

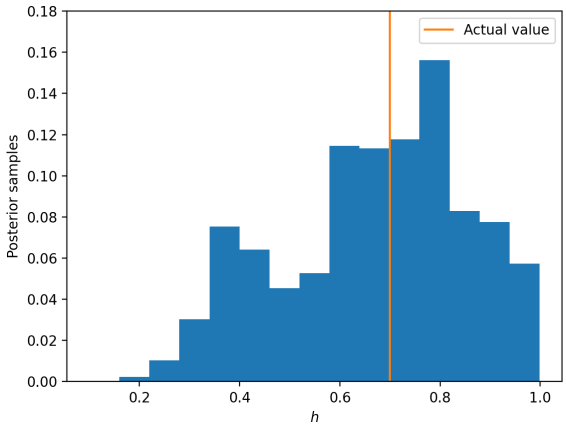

(a) Weighted samples of the Hubble parameter $h = 0.7$ Resulting in $h = 0.67 \pm 0.18$. The samples converged better than when using $\mathcal{M}_z$

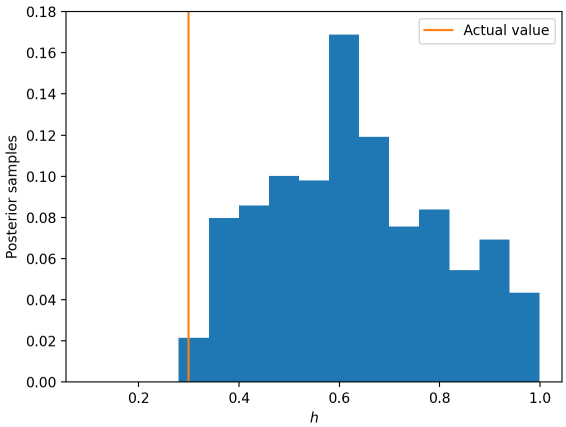

(b) Weighted samples for the Hubble parameter, where $h = 0.3$. The inferred value was $h = 0.63 \pm 0.17$, which is still too large, however there is a clear difference to fig. 5.7 (a).

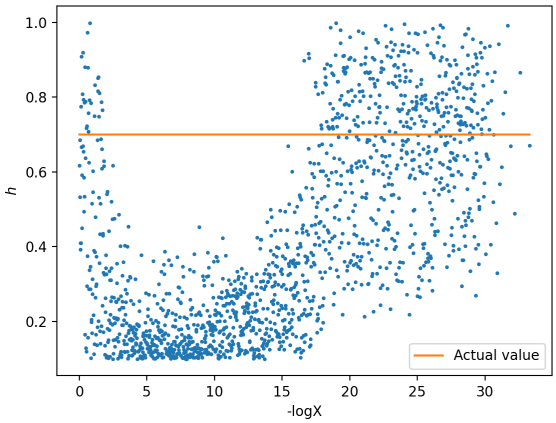

(c) Evolution of Hubble parameter for $h = 0.7$

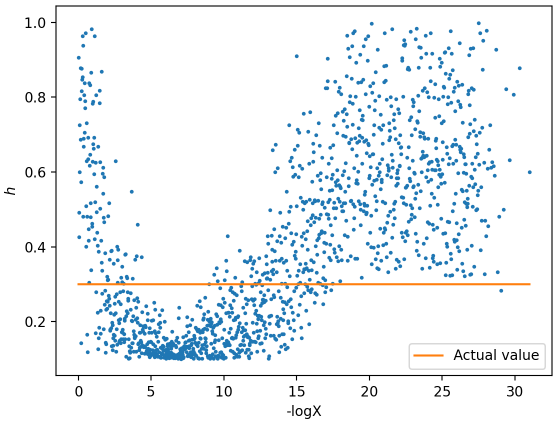

(d) Evolution of Hubble parameter for $h = 0.3$

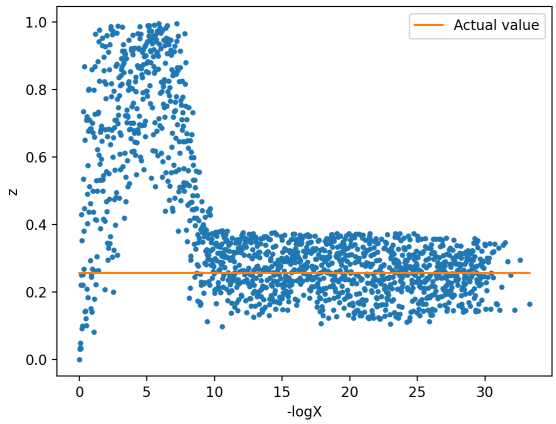

(e) Evolution of redshift, which seems to convergesbefore the Hubble parameter does

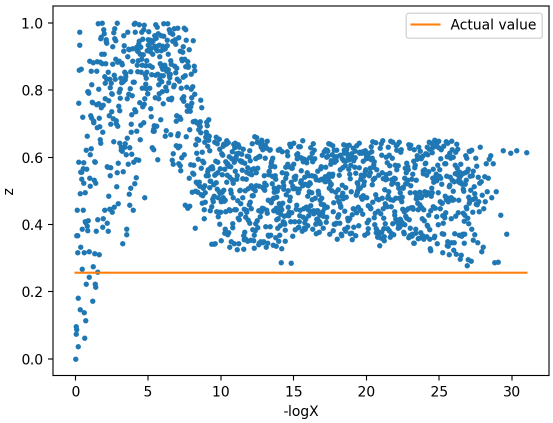

(f) Evolution of redshift. There is clearly an overestimation of the redshift in this case

Figure 5.7: Results for a dark event sampling $\mathcal{M}_c$ instead of $\mathcal{M}_z$, both use the same parameters, however in plots (a), (c) and (e) the Hubble parameter was set to $h = 0.7$ and for (b), (d) and (f) it was set to $h = 0.3$. Clearly the results are better when $\mathcal{M}_c$ is sampled instead of $\mathcal{M}_z$ however there is still clearly an overestimation of the Hubble parameter

Gravitational Wave Events with an Electromagnetic Counterpart

As with [Abbott et al., 2021a] there are difficulties regarding dark events, however GW170817 had an EM counterpart, therefore one could use this counterpart for measuring the redshift z. This means that only h will determine the luminosity distance [8], meaning it is easier to constrain the Hubble parameter. In fig. 5.8 the results were plotted assuming a binary neutron star merger with an EM counterpart.[9] For this event the residuals have also been greatly improved as can be seen in fig. 5.9. In tab. 5.2 the results of our analysis of a GW event with an EM counterpart are shown.

[8] Currently only Binary Neutron Star mergers have a counterpart. As BNS mergers have small amplitudes this means the luminosity distance will also have to be small in order to be measurable. At short distances cosmological parameters other than the Hubble parameter have a small influence on the measured redshift.

[9] These results are quite similar to the ones found in [Abbott et al., 2021a]. Where they measured $h = 0.68^{+0.18}_{-0.08}$ using the data from GW170817.

	Run I BNS		Run II BNS	
	Input	Results	Input	Results
α(rad)	4.01	–	3.53	–
δ(rad)	0.167	–	0.55	–
z	0.021	–	0.017	–
$\mathcal{M}_z(M_\odot)$	1.18612	1.18611 ± 0.00013	1.05634	1.05634 ± 0.00015
h	0.7	$0.74^{+0.11}_{-0.31}$	0.7	$0.64^{+0.11}_{-0.31}$
ψ(rad)	0.39	0.77 ± 0.45	1.29	1.11 ± 0.35
ι(rad)	0.70	0.69 ± 0.24	1.25	0.99 ± 0.32
$t_c(s)$ (s)	0	0.00000 ± 0.00011	0	0.00000 ± 0.00018
ϕ_c(rad)	4.43	3.64 ± 0.92	3.52	3.84 ± 0.74

Table 5.2: The data obtained from two runs. The given standard deviation is the standard deviation of the probability distribution.

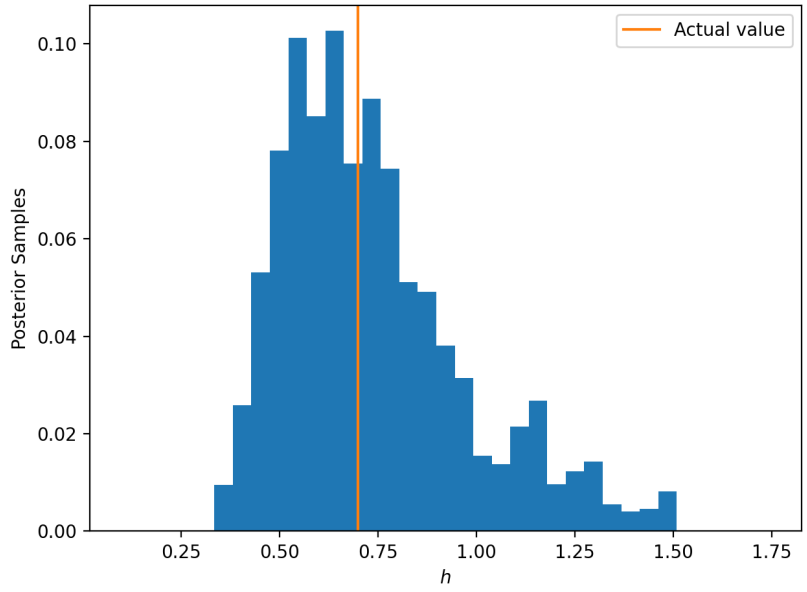

Figure 5.8: Results for Hubble parameter measurement of a binary neutron star merger with an EM counterpart.

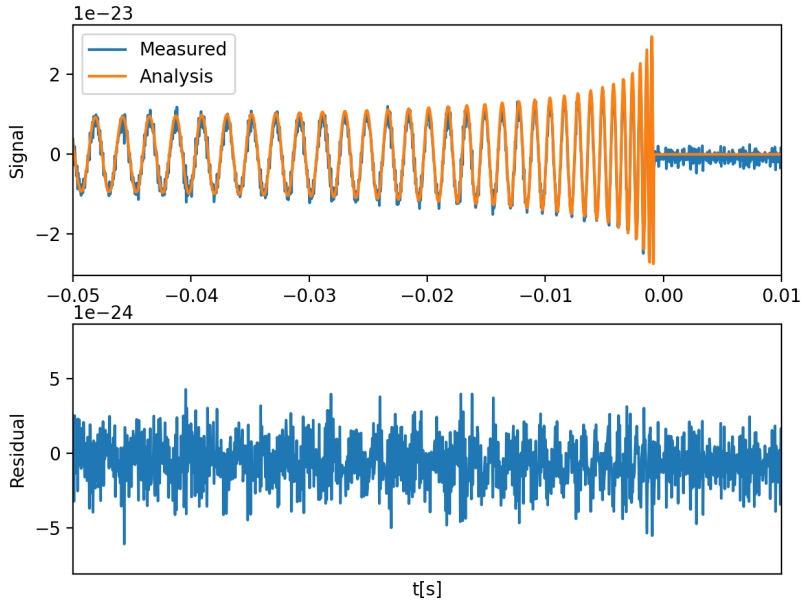

Figure 5.9: Residuals for Binary Neutron Star Merger. All parameters have been determined well therefore there is little change during and after the signal

5.4 *Combining Results*

Events with a counterpart give us by far the best results, however these results can be improved if the results from independent measurements are combined. To do this the algorithm outlined in[10] is used. Assuming N independent measurements $d_1 \dots d_N$ and a parameter λ one wishes to determine, one can use Bayes' theorem to obtain

$$p(\lambda \mid d_1, \dots, d_N) \propto p(\lambda) \cdot p(d_1, \dots, d_N \mid \lambda) \tag{5.3}$$

As the measurements are independent one can use the chain rule and rewrite this as

$$p(\lambda \mid d_1, \dots, d_N) \propto p(\lambda) \prod_{i=1}^{N} p(d_i \mid \lambda) \tag{5.4}$$

where

$$p(d_i \mid \lambda) = \int p(\vec{\theta}) p(d_i \mid \vec{\theta}, \lambda) \tag{5.5}$$

In this case $\vec{\theta}$ are all parameters but the Hubble parameter. To approximate the posterior distribution a weighted histogram is used with the weights described earlier and N_{bin}. Assigning a probability p_i to each bin is done using the Dirichlet distribution, assuming bin i has m_i samples multiplied with their respective weights. The total distribution p can be described as

$$p(\vec{p}, \vec{m}) = \frac{1}{Z(\vec{m})} \prod_{i=1}^{N_{bin}} p_i^{m_i - 1} \tag{5.6}$$

[10] Walter Del Pozzo, John Veitch, and Alberto Vecchio. Testing general relativity using Bayesian model selection: Applications to observations of gravitational waves from compact binary systems. *Physical Review D*, 83(8), Apr 2011. DOI: 10.1103/PhysRevD.83.082002

The normalisation constant $Z(\vec{m})$ is given by

$$Z(\vec{m}) = \frac{\prod_{i=1}^{N_{bin}} \Gamma(m_i)}{\Gamma(\sum_{i=1}^{N_{bin}} m_i)} \tag{5.7}$$

The probabilities are calculated using Scipy [11]. Histograms can then be multiplied by multiplying the probabilities p_i of one histogram with the probabilities of another histogram p_i'. In fig. 5.10 the combination of two events with an EM counterpart is shown. The results for the individual events were $h = 0.74^{+0.11}_{-0.31}$ and $h = 0.64^{+0.11}_{-0.31}$ for event (a) and (b) respectively. If combined this resulted in $h = 0.64^{+0.11}_{-0.16}$ Due to the fact that there are a limited number of samples in order to keep the runtime down, there are bins where there aren't as many samples as one would ideally like, meaning the distribution isn't continuous. This will have an effect on the confidence intervals one calculates. When comparing our results to [12], then our confidence intervals are larger. This can partially be due to the relatively low number of samples and discontinuities as bins that ideally would not have been included in the confidence interval now have been.

[11] Scipy is a python package, which can automatically calculate the probabilities $\vec{p}$ needed.

[12] B. P. Abbott, R. Abbott, T. D. Abbott, S. Abraham, F. Acernese, and et al. A Gravitational-wave Measurement of the Hubble Constant Following the Second Observing Run of Advanced LIGO and Virgo. *The Astrophysical Journal*, 909(2):218, Mar 2021a. DOI: 10.3847/1538-4357/abdcb7

5.5 Conclusion

This work discussed how gravitational waves work and how these are detected. Using an analytical model approximating the inspiral phase of binary compact objects and generated noise it was possible to produce realistic signals which could then be used for analysis. Due to increased sensitivity Einstein Telescope will be able to measure gravitational waves with much precision than current detectors, this means one can determine the parameters more precisely. The redshifted chirp mass and the time of coalescence could be determined most precisely as the frequency depends only on these parameters. The angular precision gave relatively good results however the precision varied. Also the luminosity distance seems to be inferred more precisely with the network used. Inclination, phase and angle of polarisation could all be determined, however with varying precision depending on the parameter. Determining the redshift using dark events has proven to be a challenge and we were mostly unable to determine the redshift which is necessary to determine the Hubble parameter. Using an event with an EM counterpart it was possible to determine the Hubble parameter and by combining two measurements it is possible to increase the precision of this result. Calculating other cosmological parameters such as Ω_m or Ω_λ could not be done using this method.

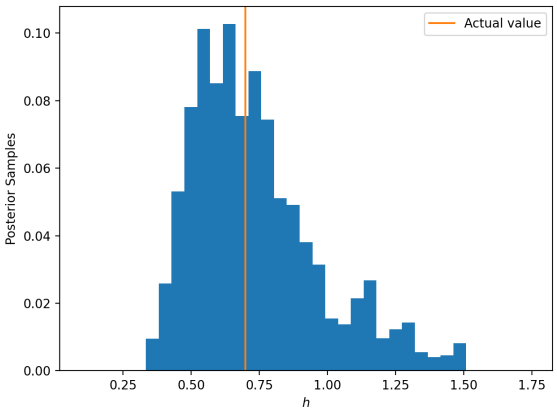

(a) Weighted samples for the Hubble parameter for the first event with an EM counterpart

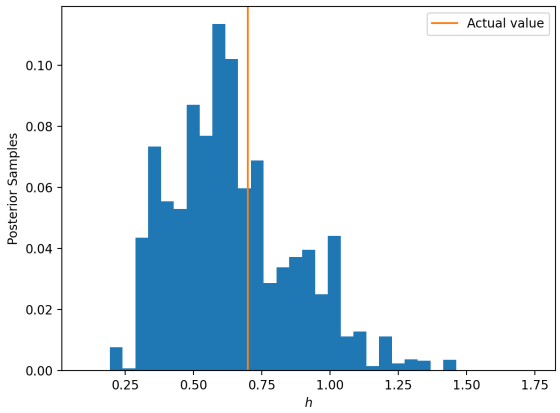

(b) Weighted samples for the Hubble parameter for the second event with an EM counterpart

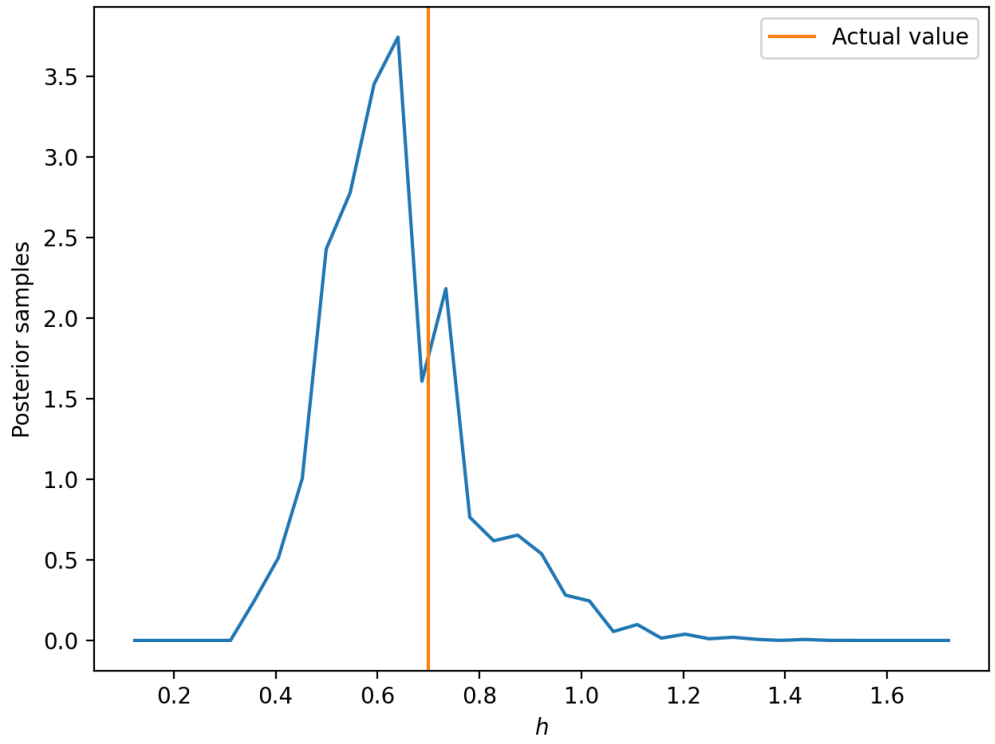

(c) Combined posterior probability for two events, Due to a relatively low number of samples the distribution is not totally continuous

Figure 5.10: Combination of two Events with Counterparts

Acknowledgements

I would like to thank Prof. Hebbeker for the opportunity to write this thesis about this very interesting subject, also I would like to thank Prof. Stahl for being the second corrector of this work. Next, to thank the people who have supervised my work, I would like to thank Robert Joppe and Tim Kuhlbush for their patience, insight and other ways to help me. Also I would like to thank Robert for proofreading this thesis and giving many tips to improve it. Furthermore I would like to thank Prof. Del Pozzo and the other members from the ET group of the RWTH, especially Markus Bachlechner, for their help. Finally I would like to thank my family for their support.

Bibliography

B. P. Abbott, R. Abbott, T. D. Abbott, M. R. Abernathy, and F. et al. Acernese. The basic physics of the binary black hole merger GW150914. *Annalen der Physik*, 529(1-2):1600209, Oct 2016. DOI: 10.1002/andp.201600209.

B. P. Abbott, R. Abbott, T. D. Abbott, S. Abraham, F. Acernese, and et al. A Gravitational-wave Measurement of the Hubble Constant Following the Second Observing Run of Advanced LIGO and Virgo. *The Astrophysical Journal*, 909(2):218, Mar 2021a. DOI: 10.3847/1538-4357/abdcb7.

R. Abbott, T. D. Abbott, S. Abraham, F. Acernese, K. Ackley, and et al. GWTC-2: Compact Binary Coalescences Observed by LIGO and Virgo during the First Half of the Third Observing Run. *Physical Review X*, 11(2), Jun 2021b. DOI: 10.1103/PhysRevX.11.021053.

N. Aghanim, Y. Akrami, M. Ashdown, J. Aumont, C. Baccigalupi, and et al. Planck 2018 results. *Astronomy and Astrophysics*, 641:A6, Sep 2020. DOI: 10.1051/0004-6361/201833910.

Bruce Allen. Gravitational Wave Detector Sites. arXiv:gr-qc/9607075v1, Jul 1996.

Jon Louis Bentley. Multidimensional Binary Search Trees Used for Associative Searching. *Commun. ACM*, 18(9):509–517, Sep 1975. DOI: 10.1145/361002.361007.

Timo Butz. Lokalisierung von Gravitationswellensignalen durch Zeit- & Amplitudeninformation mit dem Einstein-Teleskop. Master's thesis, RWTH-Aachen, Jul 2020. URL https://www.institut3b.physik.rwth-aachen.de/cms/ParticlePhysics3B/Forschung/Einstein-Telekop/~jabyq/Fertige-Abschlussarbeiten/lidx/1/.

LIGO Scientific Collaboration. Observation of Gravitational Waves from a Binary Black Hole Merger. *Physical Review Letters*, 116(6), Feb 2016. DOI: 10.1103/PhysRevLett.116.061102.

Walter Del Pozzo, John Veitch, and Alberto Vecchio. Testing general relativity using Bayesian model selection: Applications to observations of gravitational waves from compact binary systems. *Physical Review D*, 83(8), Apr 2011. DOI: 10.1103/PhysRevD.83.082002.

Scott Dodelson. *Modern cosmology*. Academic Press, 2003.

Albert Einstein. Die Feldgleichungen der Gravitation. *Sitzungsberichte der Königlich Preußischen Akademie der Wissenschaften Berlin*, pages 844–847, Jan 1915.

Albert Einstein. Über Gravitationswellen. *Sitzungsberichte der Königlich Preußischen Akademie der Wissenschaften (Berlin)*, pages 154–167, Jan 1918.

ESA/Planck Collaboration. URL https://sci.esa.int/s/W3kNpXW. Accessed: 10-Aug-2021.

ET steering committee. ET design report update 2020. Technical report, Nov 2020.

Gary J. Feldman and Robert D. Cousins. A Unified Approach to the Classical Statistical Analysis of Small Signals. *Physical Review D*, 57 (7):3873–3889, Apr 1998. DOI: 10.1103/PhysRevD.57.3873.

F. Feroz, M. P. Hobson, and M. Bridges. MultiNest: an efficient and robust Bayesian inference tool for cosmology and particle physics. *Monthly Notices of the Royal Astronomical Society*, 398(4):1601–1614, Oct 2009. DOI: 10.1111/j.1365-2966.2009.14548.

Lee S. Finn. Detection, measurement, and gravitational radiation. *Phys. Rev. D*, 46:5236–5249, Dec 1992. DOI: 10.1103/PhysRevD.46.5236.

Wendy L. Freedman, Barry F. Madore, Brad K. Gibson, Laura Ferrarese, Daniel D. Kelson, and et al. Final Results from the Hubble Space Telescope Key Project to Measure the Hubble Constant. *The Astrophysical Journal*, 553(1):47–72, May 2001. DOI: 10.1086/320638.

A. Friedmann. Über die Krümmung des Raumes. *Zeitschrift für Physik*, 10(1):377–386, Dec 1922. DOI: 10.1007/BF01332580.

Jonas Hellrung. Lokalisierung von kollidierenden neutronensternen mit dem einstein-teleskop. Master's thesis, RWTH-Aachen, Jul 2020. URL https://www.institut3b.physik.rwth-aachen.de/cms/ParticlePhysics3B/Forschung/Einstein-Telekop/~jabyq/Fertige-Abschlussarbeiten/lidx/1/.

D. E. Holz and S. A. Hughes. Using Gravitational-Wave Standard Sirens. *The Astrophysical Journal*, 629(1):15–22, Aug 2005. DOI: 10.1086/431341.

Edwin Hubble. A Relation Between Distance and Radial Velocity Among Extra-Galactic Nebulae. *Proceedings of the National Academy of Sciences*, 15(3):168–173, Mar 1929. DOI: 10.1073/pnas.15.3.168.

J. Huchra. URL lweb.cfa.harvard.edu/~dfabricant/huchra/hubble/. Accessed: 10-Aug-2021.

Piotr Jaranowski, Andrzej Królak, and Bernard F. Schutz. Data analysis of gravitational-wave signals from spinning neutron stars: The signal and its detection. *Physical Review D*, 58(6), Aug 1998. DOI: 10.1103/PhysRevD.58.063001.

G. Lemaître. Un Univers homogène de masse constante et de rayon croissant rendant compte de la vitesse radiale des nébuleuses extra-galactiques. *Annales de la Société Scientifique de Bruxelles*, 47:49–59, Jan 1927.

Mark Meckes. Covariance of points distributed in a n-ball. URL https://mathoverflow.net/q/35302. Accessed: 10 Aug 2021.

C. J. Moore, R. H. Cole, and C. P. L. Berry. Gravitational-wave sensitivity curves. *Classical and Quantum Gravity*, Dec 2014. DOI: 10.1088/0264-9381/32/1/015014.

E. Poisson and C.M. Will. Gravitational waves from inspiraling compact binaries: Parameter estimation using second-post-Newtonian waveforms. *Phys. Rev. D*, 52(2):848–855, Jul 1995. DOI: 10.1103/PhysRevD.52.848.

W. Del Pozzo. Inference of the cosmological parameters from gravitational waves: application to second generation interferometers Inference of the cosmological parameters from gravitational waves: application to second generation interferometers. Arxiv:1108.1317v3, Aug 2012.

Adam G. Riess, Stefano Casertano, Wenlong Yuan, Lucas M. Macri, and Dan Scolnic. Large Magellanic Cloud Cepheid Standards Provide a 1the Determination of the Hubble Constant and Stronger Evidence for Physics beyond Lambda CDM. *The Astrophysical Journal*, 876(1), May 2019. DOI: 10.3847/1538-4357/ab14422.

H. P. Robertson. Kinematics and World-Structure. *The Astrophysical Journal*, 82:284, Nov 1935. DOI: 10.1086/143681.

B. Schutz. *A First Course in General Relativity*. Cambridge University Press, 2009.

Bernard F. Schutz. Determining the Hubble constant from gravitational wave observations. *Nature*, 323(6086):310–311, Sep 1986. DOI: 10.1038/323310a0.

Neha Singh and Tomasz Bulik. Constraining parameters of coalescing stellar mass binary black hole systems with Einstein Telescope alone. arXiv:2011.06336 astro-ph.HE, Nov 2020.

J. Skilling. Nested sampling for general Bayesian computation. *Bayesian Analysis*, (4):833 – 859, Dec 2006. DOI: 10.1214/06-BA127.

Joshua S Speagle. dynesty: a dynamic nested sampling package for estimating Bayesian posteriors and evidences. *Monthly Notices of the Royal Astronomical Society*, 493(3):3132–3158, Feb 2020. DOI: 10.1093/mnras/staa278.

M. Spurio. An introduction to astrophysical observables in gravitational wave detections. arXiv:1906.03643v1, Jul 2019.

A. G. Walker. On Milne's Theory of World-Structure. *Proceedings of the London Mathematical Society*, s2-42(1):90–127, Jan 1937. DOI: 10.1112/plms/s2-42.1.90.

Steven Weinberg. *Cosmology*. Oxford University Press, 2008.

Note

Due to a typo the luminosity distance is calculated using $c = 299892458$. This will not have an influence on the results as this is only a 0.03% deviation and the luminosity distance can't be determined this precisely.

Appendix A: KD cluster

When creating multiple ellipses one wishes to group points which are close together so to minimise the volumes of the respective ellipses. To do this the kd cluster algorithm was used[13]. Usually one starts this algorithm with two random points, however as having already calculated a bounding matrix for all points, therefore the major axis endpoints can be calculated, which will be called S_1 and S_2.[14] Then the distance d_i from both points S_i to the centre of our ellipsoid is calculated for each point and sorted to one of the two points S_i with the shortest distance. After all points have been clustered, both S_i are updated where the new S_i are the means of both clusters. This is then repeated several times. This gives two clusters with minimal overlap.

[13] Not to be mistaken with the kd tree algorithm used to search galaxies

[14] For more information on how to calculate these endpoints see dynesty

Appendix B: Angular Precision of Run II

In ch. 5 the results were shown for two dark events and the angular precision of one event. In fig. B1 we wish to show the angular precision plot of the other event. As the samples converged rather late in this case towards to actual value the confidence intervals are relatively large. The reason why the samples converged later in this case will have to do with the fact that the amplitude was significantly smaller, meaning the difference in likelihood caused by a wrong point of origin are not as dire as for an event with a high signal-to-noise ratio.

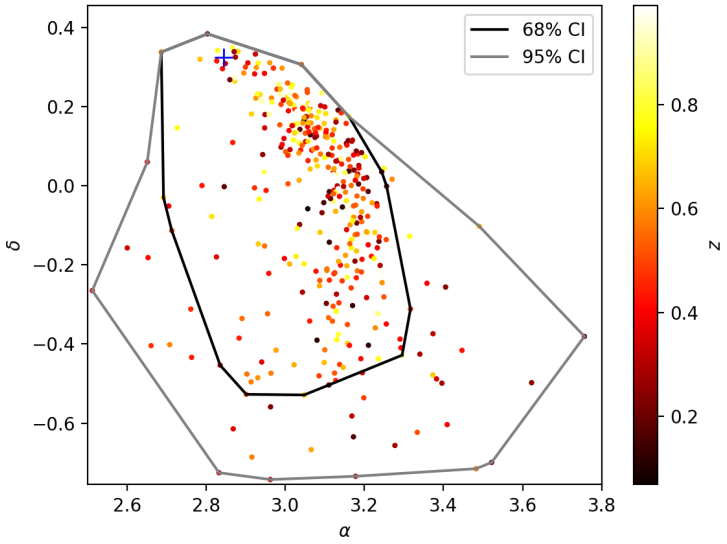

Figure B1: The angular precision plot for event II from sec. 5.2. The contours correspond to the confidence intervals. For this plot the galaxies in the SDSS catalogue have not been plotted as coverage is extremely good in this region and one would not be able to identify confidence intervals or the point of origin. The blue cross signifies the point of origin.

List of Figures

List of Tables